Semi-Discrete Central-Upwind Schemes for Elasticity in Heterogeneous Media

Alexander Kurganov* and Michael Pollack†

Abstract

We develop new central-upwind schemes for nonlinear elasticity equations in a heterogeneous medium. Finite volume central-upwind schemes consist of three steps: reconstruction, evolution, and projection onto the original grid. In our new method, the evolution is performed in the standard way by integrating the system over the space-time control volumes. However, the reconstruction and projection are performed in a special manner by taking into account the fact that the conservative variables (strain and momentum) are discontinuous across the material interfaces, while the flux variables (velocity and strain) are continuous across these material interfaces. The new reconstruction and projection procedures lead to the central-upwind scheme with extremely small numerical diffusion so that in long time calculations, the new scheme outperforms existing upwind alternatives. In addition, the proposed scheme can be made positivity preserving. To achieve this goal, the system is rewritten in terms of auxiliary variables and the local propagation speeds of the system are adjusted accordingly. Our numerical experiments demonstrate that the developed scheme is capable of accurately resolving waves with dispersive behavior that over a long period of time evolve into solitary waves while remaining nonnegative.

Key words: Hyperbolic systems of conservation laws, central-upwind schemes, nonlinear elasticity, heterogeneous media, waves with dispersive behavior, solitary waves.

1 Introduction

Consider the one-dimensional (1-D) elasticity system

$$\begin{aligned} \varepsilon_t - u_x &= 0,\\ (\rho(x)u)_t - \sigma_x(K(x);\varepsilon) &= 0, \end{aligned} \tag{1.1}$$

where $\varepsilon(x,t)$ is the strain, $u(x,t)$ is the velocity, $\rho(x)$ is the density, $K(x)$ is the bulk modulus of compressibility, and $\sigma(K(x);\varepsilon)$ is the stress. If $\rho(x)$ and $K(x)$ are both constants, than the medium is homogeneous. A nonconstant $\rho(x)$ and $K(x)$ correspond to a heterogeneous

*Mathematics Department, Tulane University, New Orleans, LA 70118, USA; kurganov@math.tulane.edu
†Mathematics Department, Tulane University, New Orleans, LA 70118, USA; mpollack@tulane.edu

medium. We consider a layered medium consisting of two different materials of length ℓ with densities ρ_1 and ρ_2 and bulk moduluses of compressibility K_1 and K_2 so that for all integer j,

$$\rho(x)=\begin{cases}\rho_1, & \text{if } 2j\ell<x<(2j+1)\ell,\\ \rho_2, & \text{otherwise,}\end{cases} \tag{1.2}$$

$$K(x)=\begin{cases}K_1, & \text{if } 2j\ell<x<(2j+1)\ell,\\ K_2, & \text{otherwise.}\end{cases} \tag{1.3}$$

The stress-strain relation in the linear case has the form $\sigma_i(\varepsilon)=K_i\varepsilon,\ i=1,2$. A more realistic model is obtained when a nonlinear stress-strain relation is considered. We take

$$\sigma_i(\varepsilon)=K_i\varepsilon+\beta K_i^2\varepsilon^2,\quad i\in\{1,2\},\qquad \beta=\text{Const} \tag{1.4}$$

or

$$\sigma_i(\varepsilon)=e^{K_i\varepsilon}-1,\quad i\in\{1,2\} \tag{1.5}$$

as examples of such relations (see [10, 19–22]). In a homogeneous medium with a nonlinear stress-strain relation, a generic solution of (1.1) and (1.4) will typically develop shock and rarefaction waves. But in a heterogeneous medium with a nonlinear stress-strain relation, the resulting waves will have dispersive behaviors that will lead to solitary waves instead of shock waves [10, 18–22].

The elasticity system (1.1) can be put into the framework of conservation laws with space-dependent flux. To this end, we rewrite (1.1) as

$$\mathbf{q}_t+\mathbf{f}\left(\mathbf{C}(x);\mathbf{q}\right)_x=\mathbf{0}, \tag{1.6}$$

where

$$\mathbf{q}=\begin{pmatrix}\varepsilon\\ m\end{pmatrix},\quad \mathbf{f}\left(\mathbf{C}(x);\mathbf{q}\right)=\begin{pmatrix}-m/\rho\\ -\sigma\end{pmatrix},$$

and $m=\rho u$ denotes the momentum.

Since (1.6) is a hyperbolic system of conservation laws, it is very natural to solve (1.6) numerically by a finite volume Godunov-type scheme. These schemes form a class of projection-evolution methods in which the solution is first approximated by a global piecewise polynomial function and than evolved in time according to the integral form of (1.6):

$$\begin{aligned}\frac{1}{\Delta x}\int\limits_{x-\frac{\Delta x}{2}}^{x+\frac{\Delta x}{2}}\mathbf{q}(\xi,t+\Delta t)\,d\xi&=\frac{1}{\Delta x}\int\limits_{x-\frac{\Delta x}{2}}^{x+\frac{\Delta x}{2}}\mathbf{q}(\xi,t)\,d\xi\\ &-\frac{1}{\Delta x}\int\limits_{t}^{t+\Delta t}\left[\mathbf{f}\Big(\mathbf{C}\big(x+\frac{\Delta x}{2}\big);\mathbf{q}\big(x+\frac{\Delta x}{2},\tau\big)\Big)-\mathbf{f}\Big(\mathbf{C}\big(x-\frac{\Delta x}{2}\big);\mathbf{q}\big(x-\frac{\Delta x}{2},\tau\big)\Big)\right]d\tau.\end{aligned} \tag{1.7}$$

Here, Δx and Δt are small spatial and temporal scales, respectively.

To design a second-order Godunov-type scheme, we first introduce a uniform (for simplicity) grid with $x_j=j\Delta x$ and $t^n=n\Delta t$ and assume that the numerical solution, realized in

terms of its cell averages

$$\bar{\mathbf{q}}_j^n \approx \frac{1}{\Delta x}\int\limits_{x_{j-\frac{1}{2}}}^{x_{j+\frac{1}{2}}} \mathbf{q}(x,t^n)\,dx, \tag{1.8}$$

is available at time t^n. These cell averages are then used to reconstruct a global (in space) piecewise linear interpolant, which is evolved in time via the integral equation (1.7). The latter can be done in two different ways leading to two classes of Godunov-type schemes: upwind and central.

Upwind schemes (see, e.g., [2, 4, 5, 11, 18, 30]) are obtained by sampling (1.7) at the grid points $x_j = j\Delta x$ and $t^n = n\Delta t$. Then, the time integrals in (1.7) are evaluated using the information on nonlinear, generically discontinuous waves generated at each cell interface at time t^n. This requires either exact or approximate generalized Riemann problem solver, which may be difficult (or even impossible) to derive and computationally expensive to implement.

Central schemes are a simpler alternative to the upwind methods. Within the central framework, originally developed in [27] and then extended to higher order and multiple number of space dimensions in [1,3,9,23,24,26,28], the solution is evolved using the same integral equation (1.7), but now sampled at the cell interfaces $x_{j+\frac{1}{2}} = (j+1/2)\Delta x$ so that all of the Riemann fans are contained in the corresponding control volumes. Then the solution along both the left and right sides of the control volumes is smooth (provided an appropriate CFL condition is satisfied) and the time integrals in (1.7) may be evaluated without solving any generalized Riemann problems. This makes central schemes simple, robust and efficient. A drawback of central schemes is their relatively large numerical dissipation, which makes them unsuitable for large time integrations. A way to reduce the numerical dissipation present in central schemes was proposed in [17], where the first central-upwind scheme was developed. The numerical dissipation was further reduced in [14] and [13]. The central-upwind schemes contain three steps: Reconstruction, Evolution, and Projection onto the original grid. The main idea behind the construction of central-upwind schemes is in the integration over smaller nonuniform control volumes that still contain the entire Riemann fans (this makes the central-upwind schemes to be central). The size of such control volumes is proportional to the local propagation speeds (this feature brings a certain upwind nature into the central framework). Due to the finite speed of propagation, the computational domain should now be split into "smooth" and "nonsmooth" control volumes (the latter ones are those that contain the Riemann fans), where the solution is first evolved to the new time level and then projected back onto the original grid (see [13, 14, 17] for details).

Although the central-upwind schemes were designed for the systems of conservation laws like

$$\mathbf{q}_t + \mathbf{f}(\mathbf{q})_x = \mathbf{0}, \tag{1.9}$$

they can be directly applied to the system with space-dependent fluxes (1.6). However, this will lead to a poor resolution in the case of layered material (as we demonstrate in §2.1.1 below).

We develop new central-upwind schemes for (1.1) by designing special reconstruction and projection procedures, which take into account the fact that though the conservative variables (strain and momentum) are discontinuous across the layer interfaces, the flux variables (velocity and strain) are continuous there. The resulting fully discrete central-upwind scheme

is quite complicated. However, when we pass to the semi-discrete limit (as the time step $\Delta t \to 0$), the resulting numerical flux is a quite simple modification of the central-upwind flux from [13].

The new 1-D semi-discrete central-upwind scheme is described in §2.2. It is extended to the two-dimensional (2-D) case in §3. Numerical examples presented in §4 clearly demonstrate that the developed scheme is capable of accurately resolving waves with dispersive behavior over a small time scale. The scheme performs extremely well over a long period of time as the waves with dispersive behavior evolve into solitary waves and it seems to outperform the existing methods found in [19–22].

2 One-Dimensional Central Upwind Schemes

In this section, we develop a central-upwind scheme for (1.1). In principle, one can apply the central-upwind scheme originally derived for (1.9) to the case of a space dependent flux, which we will do first.

2.1 Direct Implementation of the Scheme from [13]

In the beginning of the section, we follow the lines of [13] and derive the central-upwind scheme for the 1-D hyperbolic system of conservation laws with space-dependent flux (1.6). We first assume that at time level $t = t^n$ the cell averages $\{\bar{\mathbf{q}}_j^n\}$, defined in (1.8), are available. We then compute the cell averages at the new time level, $\{\bar{\mathbf{q}}_j^{n+1}\}$, in three steps: Reconstruction, Evolution, and Projection.

Step 1: Reconstruction
Using the cell averages $\{\bar{\mathbf{q}}_j^n\}$, we construct a second-order piecewise linear interpolant

$$\widetilde{\mathbf{q}}(x,t^n) = \sum_j \left[\bar{\mathbf{q}}_j^n + (\mathbf{q}_x)_j^n (x - x_j)\right] \chi_j(x), \tag{2.1}$$

where $\chi_j(x)$ is the characteristic function over the cell $(x_{j-\frac{1}{2}}, x_{j+\frac{1}{2}})$ and $(\mathbf{q}_x)_j^n$ are the slopes, which should approximate the values of $\mathbf{q}_x(x_j,t^n)$ with at least first order of accuracy. To make the reconstruction (2.1), the slopes are to be computed using a nonlinear limiter, see, e.g., [4,7,8,11,18,25,27,29,31]. In the numerical experiments reported below, the generalized minmod limiter [4,11,18,25,27,29,31],

$$(\mathbf{q}_x)_j^n = \text{minmod}\left(\theta\frac{\bar{\mathbf{q}}_{j+1}^n - \bar{\mathbf{q}}_j^n}{\Delta x}, \frac{\bar{\mathbf{q}}_{j+1}^n - \bar{\mathbf{q}}_{j-1}^n}{2\Delta x}, \theta\frac{\bar{\mathbf{q}}_j^n - \bar{\mathbf{q}}_{j-1}^n}{\Delta x}\right),$$

has been applied in a componentwise manner. Here,

$$\text{minmod}(z_1,z_2,\ldots,z_m) = \begin{cases} \min(z_1,z_2,\ldots,z_m), & \text{if } z_i > 0 \ \forall i = 1,\ldots,m,\\ \max(z_1,z_2,\ldots,z_m), & \text{if } z_i < 0 \ \forall i = 1,\ldots,m,\\ 0, & \text{otherwise,}\end{cases}$$

and the parameter $\theta \in [1,2]$ can be used to control numerical dissipation. When $\theta = 1$, the minmod reconstruction (and thus the resulting scheme) is most dissipative and when $\theta = 2$,

the minmod reconstruction is least dissipative. In what follows, we will refer to the minmod reconstruction with $\theta = 2$ as the MinMod2 reconstruction.

Step 2: Evolution

We next need to evolve the approximate solution, represented by a global piecewise linear interpolant $\widetilde{\mathbf{q}}(x,t^n)$, to the next time level using the integral form of the conservation law (1.7). To this end, we first estimate the local speeds of propagation:

$$\begin{aligned} a^+_{j+\frac12} &= \max\left\{\lambda_+\Big(\frac{\partial\mathbf{f}}{\partial\mathbf{q}}\big(\mathbf{C}^-_{j+\frac12};\mathbf{q}^-_{j+\frac12}\big)\Big),\ \lambda_+\Big(\frac{\partial\mathbf{f}}{\partial\mathbf{q}}\big(\mathbf{C}^+_{j+\frac12};\mathbf{q}^+_{j+\frac12}\big)\Big),0\right\}\\ a^-_{j+\frac12} &= \min\left\{\lambda_-\Big(\frac{\partial\mathbf{f}}{\partial\mathbf{q}}\big(\mathbf{C}^-_{j+\frac12};\mathbf{q}^-_{j+\frac12}\big)\Big),\ \lambda_-\Big(\frac{\partial\mathbf{f}}{\partial\mathbf{q}}\big(\mathbf{C}^+_{j+\frac12};\mathbf{q}^+_{j+\frac12}\big)\Big),0\right\}, \end{aligned} \tag{2.2}$$

where $\lambda_+ > \lambda_-$ are the eigenvalues of the Jacobian $\frac{\partial\mathbf{f}}{\partial\mathbf{q}}$, and compute the left- and right-sided point values of $\mathbf{C}$ and of the interpolant $\widetilde{\mathbf{q}}(x,t^n)$ at $x = x_{j+\frac12}$:

$$\mathbf{C}^\pm_{j+\frac12} = \mathbf{C}(x_{j+\frac12}\pm 0),\quad \mathbf{q}^+_{j+\frac12} = \bar{\mathbf{q}}^n_{j+1} - \frac{\Delta x}{2}(\mathbf{q}_x)^n_{j+1},\quad \mathbf{q}^-_{j+\frac12} = \bar{\mathbf{q}}^n_j + \frac{\Delta x}{2}(\mathbf{q}_x)^n_j, \tag{2.3}$$

respectively. Note that if $\mathbf{C}$ is continuous at $x_{j+\frac12}$, then $\mathbf{C}^+_{j+\frac12} = \mathbf{C}^-_{j-\frac12}$, but the case of a discontinuous $\mathbf{C}$ is generic. In order to deal with this, we build the grid such that the discontinuities of $\mathbf{C}$ occur at the cell interfaces.

For the system (1.1), the Jacobian is

$$\frac{\partial\mathbf{f}}{\partial\mathbf{q}} = \begin{pmatrix} 0 & -\dfrac{1}{\rho(x)}\\[2ex] -\dfrac{d\sigma}{d\varepsilon} & 0\end{pmatrix}.$$

Its eigenvalues are

$$\lambda_\pm(x;\varepsilon) = \pm\sqrt{\frac{d\sigma/d\varepsilon}{\rho(x)}},$$

where for σ given by (1.4),

$$\frac{d\sigma}{d\varepsilon} = K(x) + 2\beta K^2(x)\varepsilon, \tag{2.4}$$

while for σ given by (1.5),

$$\frac{d\sigma}{d\varepsilon} = K(x)e^{K(x)\varepsilon}. \tag{2.5}$$

Since the Riemann fan for the system (1.1) is symmetric, we have $a^+_{j+\frac12} = -a^-_{j+\frac12} =: a_{j+\frac12}$. Note that in the case of a general system (1.6), one may still define

$$a_{j+\frac12} := \max(a^+_{j+\frac12}, -a^-_{j-\frac12}). \tag{2.6}$$

We next introduce the points

$$x^n_{j+\frac12,\ell} := x_{j+\frac12} - a_{j+\frac12}\Delta t,\qquad x^n_{j+\frac12,r} := x_{j+\frac12} + a_{j+\frac12}\Delta t,$$

and notice that the Riemann fan generated at time $t=t^n$ at the cell interface $x=x_{j+\frac12}$ will remain inside the "nonsmooth" control volume $I^n_{j+\frac12}:=[x^n_{j+\frac12,\ell},x^n_{j+\frac12,r}]\times[t^n,t^{n+1}]$. Therefore, we can integrate the system (1.6) over $I^n_{j+\frac12}$ and obtain an integral equation analogous to (1.7), the time integral in which can be evaluated using the midpoint rule. This will result in the following cell average at time $t=t^{n+1}$:

$$\begin{aligned}\bar{\mathbf{q}}^{\rm int}_{j+\frac12}&=\frac{\bar{\mathbf{q}}^n_j+\bar{\mathbf{q}}^n_{j+1}}{2}+\frac{\Delta x-a_{j+\frac12}\Delta t}{4}\left((\mathbf{q}_x)^n_j-(\mathbf{q}_x)^n_{j+1}\right)\\&\quad-\frac{1}{2a_{j+\frac12}}\left[\mathbf{f}\left(\mathbf{C}\big(x^n_{j+\frac12,r}\big);\mathbf{q}^{n+\frac12}_{j+\frac12,r}\right)-\mathbf{f}\left(\mathbf{C}\big(x^n_{j+\frac12,\ell}\big);\mathbf{q}^{n+\frac12}_{j+\frac12,\ell}\right)\right],\end{aligned}\tag{2.7}$$

where the point values at $t=t^{n+\frac12}$ are obtained using the first two terms of the Taylor expansion in time,

$$\mathbf{q}^{n+\frac12}_{j+\frac12,\ell}=\mathbf{q}^n_{j+\frac12,\ell}-\frac{\Delta t}{2}\mathbf{f}\big(\mathbf{C}(x^n_{j+\frac12,\ell});\mathbf{q}^n_{j+\frac12,\ell}\big)_x=\mathbf{q}^n_{j+\frac12,\ell}-\frac{\Delta t}{2}\frac{\partial\mathbf{f}}{\partial\mathbf{q}}\Big(\mathbf{C}\big(x^n_{j+\frac12,\ell}\big);\mathbf{q}^n_{j+\frac12,\ell}\Big)\,(\mathbf{q}_x)^n_j,$$

$$\mathbf{q}^{n+\frac12}_{j+\frac12,r}=\mathbf{q}^n_{j+\frac12,r}-\frac{\Delta t}{2}\mathbf{f}\big(\mathbf{C}(x^n_{j+\frac12,r});\mathbf{q}^n_{j+\frac12,r}\big)_x=\mathbf{q}^n_{j+\frac12,r}-\frac{\Delta t}{2}\frac{\partial\mathbf{f}}{\partial\mathbf{q}}\Big(\mathbf{C}\big(x^n_{j+\frac12,r}\big);\mathbf{q}^n_{j+\frac12,r}\Big)\,(\mathbf{q}_x)^n_{j+1},$$

and

$$\begin{aligned}\mathbf{q}^n_{j+\frac12,\ell}&:=\widetilde{\mathbf{q}}\big(x^n_{j+\frac12,\ell}\big)=\bar{\mathbf{q}}^n_j+(\mathbf{q}_x)^n_j\Big(\frac{\Delta x}{2}-a_{j+\frac12}\Delta t\Big),\\\mathbf{q}^n_{j+\frac12,r}&:=\widetilde{\mathbf{q}}\big(x^n_{j+\frac12,r}\big)=\bar{\mathbf{q}}^n_{j+1}-(\mathbf{q}_x)^n_{j+1}\Big(\frac{\Delta x}{2}-a_{j+\frac12}\Delta t\Big).\end{aligned}$$

Notice that we have denoted the new cell average by $\bar{\mathbf{q}}^{\rm int}_{j+\frac12}$ rather than $\bar{\mathbf{q}}^{n+1}_{j+\frac12}$ since the cell averages $\bar{\mathbf{q}}^{\rm int}_{j+\frac12}$ obtained at this stage represent the intermediate solution over a nonuniform grid, which is yet to be projected back onto the original uniform grid.

Since the "nonsmooth" control volumes do not cover the entire computational domain, the solution must also be evolved in the remaining parts, namely, in the "smooth" control volumes $I^n_j:=[x^n_{j-\frac12,r},x^n_{j+\frac12,\ell}]\times[t^n,t^{n+1}]$. This is achieved by integrating the system (1.6) over I^n_j and approximating the resulting temporal integrals using the midpoint rule as before. The new (intermediate) cell averages over the smooth parts of the solution can be then written as

$$\begin{aligned}\bar{\mathbf{q}}^{\rm int}_j&=\bar{\mathbf{q}}^n_j+\frac{(\mathbf{q}_x)^n_j}{2}\Delta t\left(a_{j-\frac12}-a_{j+\frac12}\right)\\&\quad-\frac{\lambda}{1-\lambda\left(a_{j-\frac12}+a_{j+\frac12}\right)}\left[\mathbf{f}\left(\mathbf{C}\left(x^n_{j+\frac12,\ell}\right);\mathbf{q}^{n+\frac12}_{j+\frac12,\ell}\right)-\mathbf{f}\left(\mathbf{C}\left(x^n_{j-\frac12,r}\right);\mathbf{q}^{n+\frac12}_{j-\frac12,r}\right)\right],\end{aligned}\tag{2.8}$$

where $\lambda:=\Delta t/\Delta x$.

Step 3: Projection

We consider a piecewise linear interpolant reconstructed from the evolved intermediate cell averages:

$$\widetilde{\mathbf{q}}^{\rm int}(x)=\sum_j\left\{\left[\bar{\mathbf{q}}^{\rm int}_{j+\frac12}+(\mathbf{q}_x)^{\rm int}_{j+\frac12}(x-x_{j+\frac12})\right]\chi_{[x_{j+\frac12,\ell},x_{j+\frac12,r}]}+\bar{\mathbf{q}}^{\rm int}_j\chi_{[x_{j-\frac12,r},x_{j+\frac12,\ell}]}\right\}.$$

New solution cell averages $\{\bar{\mathbf{q}}_j^{n+1}\}$ can then be computed by projecting the interpolant back onto the original grid by averaging it over the intervals $[x_{j-\frac12}, x_{j+\frac12}]$:

$$\bar{\mathbf{q}}_j^{n+1} = \frac{1}{\Delta x}\int\limits_{x_{j-\frac12}}^{x_{j+\frac12}} \widetilde{\mathbf{q}}^{\rm int}(\xi)\,d\xi = \lambda a_{j-\frac12}\bar{\mathbf{q}}^{\rm int}_{j-\frac12} + \Big[1-\lambda(a_{j-\frac12}+a_{j+\frac12})\Big]\bar{\mathbf{q}}^{\rm int}_j + \lambda a_{j+\frac12}\bar{\mathbf{q}}^{\rm int}_{j+\frac12}$$
$$+ \frac{\Delta x}{2}\left[(\lambda a_{j-\frac12})^2(\mathbf{q}_x)^{\rm int}_{j-\frac12} - (\lambda a_{j+\frac12})^2(\mathbf{q}_x)^{\rm int}_{j+\frac12}\right], \tag{2.9}$$

where

$$\begin{aligned}(\mathbf{q}_x)^{\rm int}_{j+\frac12} &= \mathrm{minmod}\left(\frac{\bar{\mathbf{q}}^{\rm int}_{j+\frac12}-\mathbf{q}^{n+1}_{j+\frac12,\ell}}{x_{j+\frac12}-x_{j+\frac12,\ell}}, \frac{\mathbf{q}^{n+1}_{j+\frac12,r}-\bar{\mathbf{q}}^{\rm int}_{j+\frac12}}{x_{j+\frac12,r}-x_{j+\frac12}}\right)\\ &= \frac{1}{\Delta t a_{j+\frac12}}\mathrm{minmod}\left(\bar{\mathbf{q}}^{\rm int}_{j+\frac12}-\mathbf{q}^{n+1}_{j+\frac12,\ell}, \mathbf{q}^{n+1}_{j+\frac12,r}-\bar{\mathbf{q}}^{\rm int}_{j+\frac12}\right).\end{aligned} \tag{2.10}$$

This completes the derivation of the fully discrete central-upwind scheme (2.7)–(2.10). This scheme is rather cumbersome and therefore we proceed along the lines of [13] and send $\Delta t \to 0$ to obtain a much simpler semi-discrete scheme, which will be reduced to (see [13] for details)

$$\frac{d}{dt}\bar{\mathbf{q}}_j(t) = -\frac{\mathbf{H}_{j+\frac12}(t)-\mathbf{H}_{j-\frac12}(t)}{\Delta x}, \tag{2.11}$$

where the numerical fluxes are

$$\mathbf{H}_{j+\frac12}(t) = \frac{\mathbf{f}(\mathbf{C}^+_{j+\frac12};\mathbf{q}^+_{j+\frac12}) + \mathbf{f}(\mathbf{C}^-_{j+\frac12};\mathbf{q}^-_{j+\frac12})}{2} - \frac{a_{j+\frac12}}{2}\left[\left(\mathbf{q}^+_{j+\frac12}-\mathbf{q}^-_{j+\frac12}\right)-\mathbf{d}_{j+\frac12}\right]. \tag{2.12}$$

Here, $\mathbf{d}_{j+\frac12}$ is a correction term, which is a "built-in" anti-diffusion term:

$$\mathbf{d}_{j+\frac12} = \mathrm{minmod}\left(\mathbf{q}^+_{j+\frac12}-\mathbf{q}^*_{j+\frac12}, \mathbf{q}^*_{j+\frac12}-\mathbf{q}^-_{j+\frac12}\right), \tag{2.13}$$

where

$$\mathbf{q}^*_{j+\frac12} = \frac{\mathbf{q}^+_{j+\frac12}+\mathbf{q}^-_{j+\frac12}}{2} + \frac{\mathbf{f}(\mathbf{C}^+_{j+\frac12};\mathbf{q}^+_{j+\frac12}) - \mathbf{f}(\mathbf{C}^-_{j+\frac12};\mathbf{q}^-_{j+\frac12})}{2a_{j+\frac12}}. \tag{2.14}$$

Remark 2.1 The ODE system (2.11) should be solved by a stable and sufficiently accurate ODE solver. In our numerical experiments, we have used the third-order strong stability preserving (SSP) Runge-Kutta method (see [6]).

Ideally, we would like to be able to use the scheme (2.11)–(2.14), (2.2)–(2.6) as a "black-box" solver for (1.1). In the homogeneous case, a direct application leads to accurate results. However, when the scheme is applied to the heterogeneous case, the obtained results are of a poor quality. In this case, the strain develops contact discontinuities which can not be properly resolved by the scheme (2.11)–(2.14), (2.2)–(2.6). To illustrate this, we present the following numerical example.

2.1.1 Numerical Example

We now apply the scheme (2.11)–(2.14), (2.2)–(2.6) with $\theta = 2$ to the nonlinear elasticity system (1.1)–(1.4) with $\beta = 0.3$. We first consider the case of a homogeneous media when the values of the density and bulk modulus of compressibility are constants; that is, in (1.2)–(1.4) we set

$$\rho_1 \equiv \rho_2 \equiv K_1 \equiv K_2 \equiv 2.$$

We take the initial data $\mathbf{q}(x,0) = \mathbf{0}$ and the following boundary conditions:

$$u(0,t) = \begin{cases} -0.2(1+\cos(\pi(t-30)/30)), & \text{if } t \le 60, \\ 0, & \text{if } t > 60, \end{cases} \qquad \sigma(0,t) \equiv 0. \tag{2.15}$$

The obtained results are shown in Figure 2.1. As one can see, a shock wave clearly forms and it is nicely resolved by the central-upwind scheme.

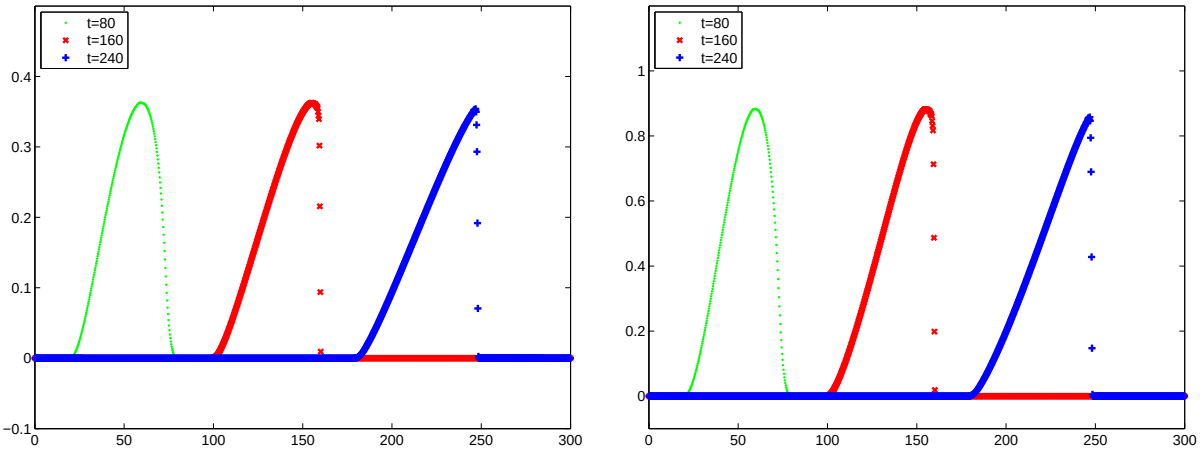

Figure 2.1: Nonlinear homogeneous elasticity. Strain (left) and stress (right) at $t = 80, 160, 240$ with $\Delta x = 0.25$ (4 grid cells per layer of material).

We next consider the heterogeneous case with the density and bulk modulus of compressibility are given by (1.2) and (1.3) with

$$\rho_1 = K_1 = 3, \quad \rho_2 = K_2 = 1, \quad \ell = 1. \tag{2.16}$$

Compared to the homogeneous case, the situation changes dramatically. In Figure 2.2, the strain and stress are computed using 4 grid cells per layer of material at $t = 80$. We compare the obtained results with the reference solution, computed by a new scheme which we derive in §2.2 (our reference solution is in very good agreement with the solution presented in [19]). As one can see, the strain is reasonably resolved while the stress is very oscillatory.

We then increase the number of grid cells per layer to 16 (see Figure 2.3). The strain is now nicely captured but the resolution of the stress has not improved. At a later time $t = 240$, both components of the solution computed with 16 grid cells per layer is of poor quality. There is a noticeable phase shift in the strain (see Figure 2.4, left) and the stress is not well resolved at all (see Figure 2.4, right).

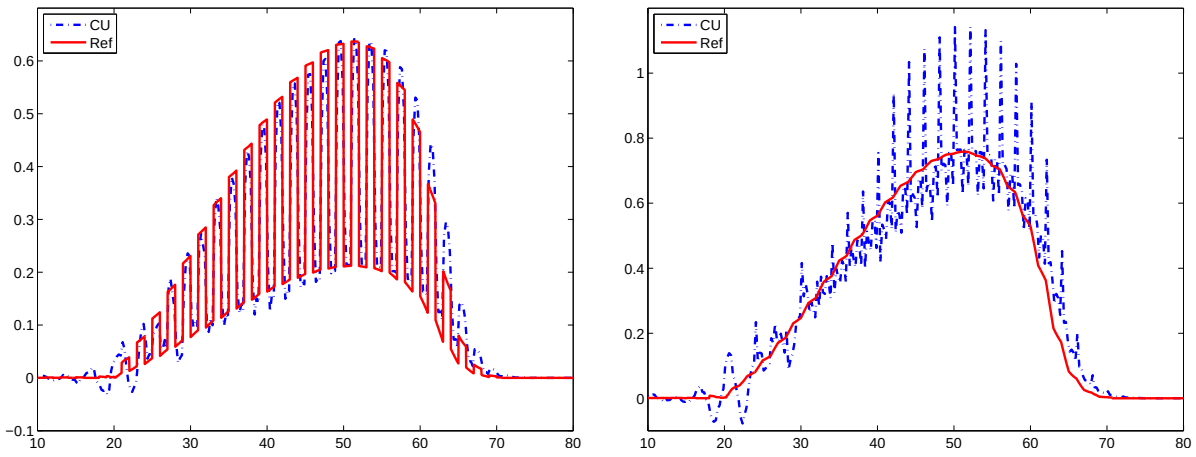

Figure 2.2: Nonlinear heterogeneous elasticity. Strain (left) and stress (right) at $t = 80$ with $\Delta x = 0.25$ (4 grid cells per layer of material) using a direct implementation of the central-upwind scheme. The solid line represents a reference solution computed by the new central-upwind scheme derived in §2.2 with $\Delta x = 0.015625$ (64 grid cells per layer of material).

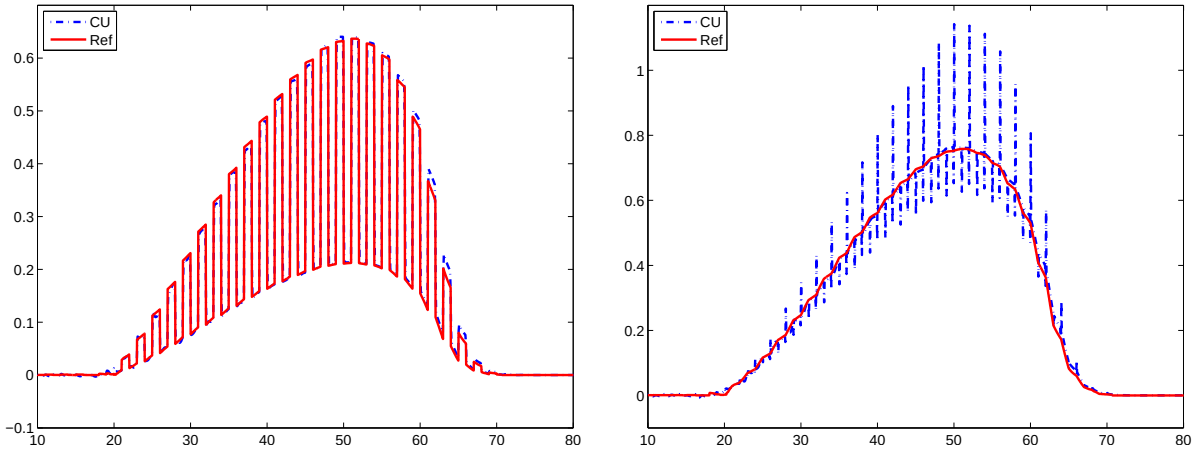

Figure 2.3: The same as in Figure 2.2, but with $\Delta x = 0.0625$ (16 grid cells per layer of material).

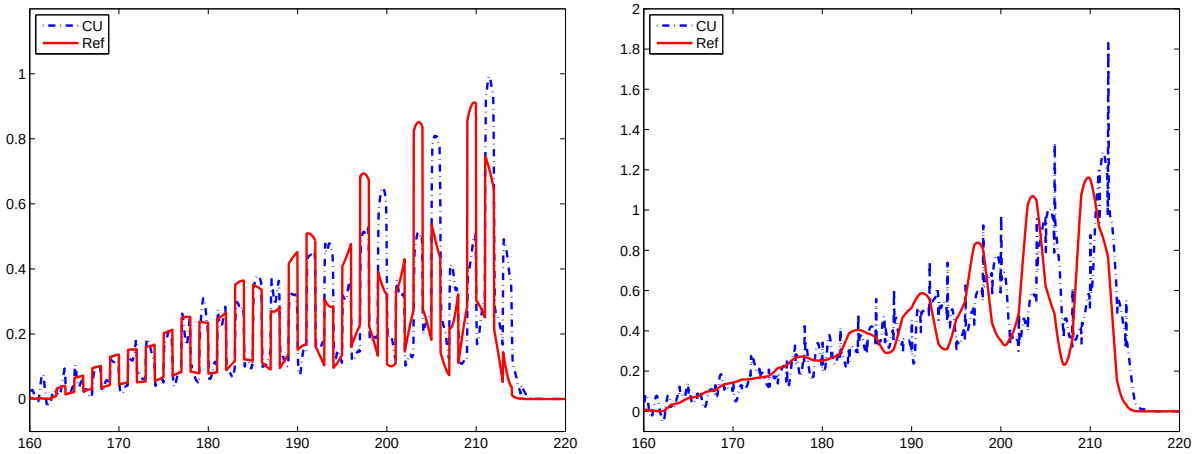

Figure 2.4: The same as in Figure 2.3, but at a later time $t = 240$.

The results reported in Figures 2.2–2.4 clearly indicate that the central-upwind scheme (2.11)–(2.14), (2.2)–(2.6) does not work properly. To rectify this, we revise the construction of the scheme by using the fact that while the conservative quantities (strain and momentum) are discontinuous across a material interface, the flux functions (velocity and stress) are continuous there. We also modify the scheme to ensure positivity of the strain and stress.

2.2 Derivation of a New Central-Upwind Scheme

In order to proceed with the derivation of the new central-upwind scheme, we first introduce a "dummy" variable $U = -\frac{u}{\varepsilon}$ and rewrite the system (1.1) as

$$\begin{aligned} \varepsilon_t + (U\varepsilon)_x &= 0, \\ (\rho U\varepsilon)_t + \sigma_x &= 0. \end{aligned} \tag{2.17}$$

The first equation in (2.17) is now a transport equation for ε. Central-upwind schemes for such equations (see, e.g., [12,15,16]) can be easily made positivity preserving. This is a reason why we prefer to work with (2.17) rather than with the original system (1.1). We will now go through the same derivation steps as in §2.1 and "fix" the problems that arise in the case of the heterogeneous elasticity system.

2.2.1 Special Reconstruction

We assume that at time t^n the cell averages $\bar{\varepsilon}_j^n$ and $\bar{m}_j^n$ are available. If we were to proceed along the lines of §2.1, then we would reconstruct piecewise linear approximations $\widetilde{\varepsilon}_j^n$ and $\widetilde{m}_j^n$. But $\bar{\varepsilon}_j^n$ and $\bar{m}_j^n$ typically jump across layer interfaces (these are contact discontinuities) so when a limiter is applied to $\bar{\varepsilon}_j^n$ and $\bar{m}_j^n$ at cells bordering a layer interface, it may result in a one-sided numerical derivative. Then, even if the resulting reconstruction of ε and m are non-oscillatory, the corresponding point values of u and σ may be oscillatory.

To illustrate such a possibility, let us consider a particular set of cell averages of m: $\{\bar{m}_{j-1} = 1.5, \bar{m}_j = 0.9, \bar{m}_{j+1} = 0.25, \bar{m}_{j+2} = 0.25\}$ and the corresponding point values of u: $\{u_{j-1} = 0.5, u_j = 0.3, u_{j+1} = 0.25, u_{j+2} = 0.25\}$, as shown in Figures 2.5 and 2.6. A MinMod2 reconstruction for m in cells j and $j+1$ is shown in Figure 2.5 (left). A layer interface is located at $x_{j+\frac{1}{2}}$ with $\rho = 3$ to the left and $\rho = 1$ to the right of the layer interface. One can see that while the reconstruction for m is non-oscillatory, the corresponding values of u, obtained through $u = m/\rho$, contain an oscillation at the layer interface, see Figure 2.5 (right).

To avoid such oscillations, we use the fact that both u and σ are continuous across a layer interface and apply the limiter to these continuous quantities rather than to ε and m. In Figure 2.6 (left), the point values $u^+_{j-\frac{1}{2}}, u^-_{j+\frac{1}{2}}, u^+_{j+\frac{1}{2}}$ and $u^-_{j+\frac{3}{2}}$ are reconstructed using MinMod2. The resulting reconstruction is non-oscillatory and the obtained values of $m = \rho u$ are non-oscillatory as well, see Figure 2.6 (right).

In the general case, the point values u_j^n and σ_j^n are

$$u_j^n = \frac{\bar{m}_j^n}{\rho_j}, \quad \sigma_j^n = K_j\bar{\varepsilon}_j^n + \beta K_j^2(\bar{\varepsilon}_j^n)^2 \quad \text{or} \quad \sigma_j^n = e^{K_j\bar{\varepsilon}_j^n} - 1,$$

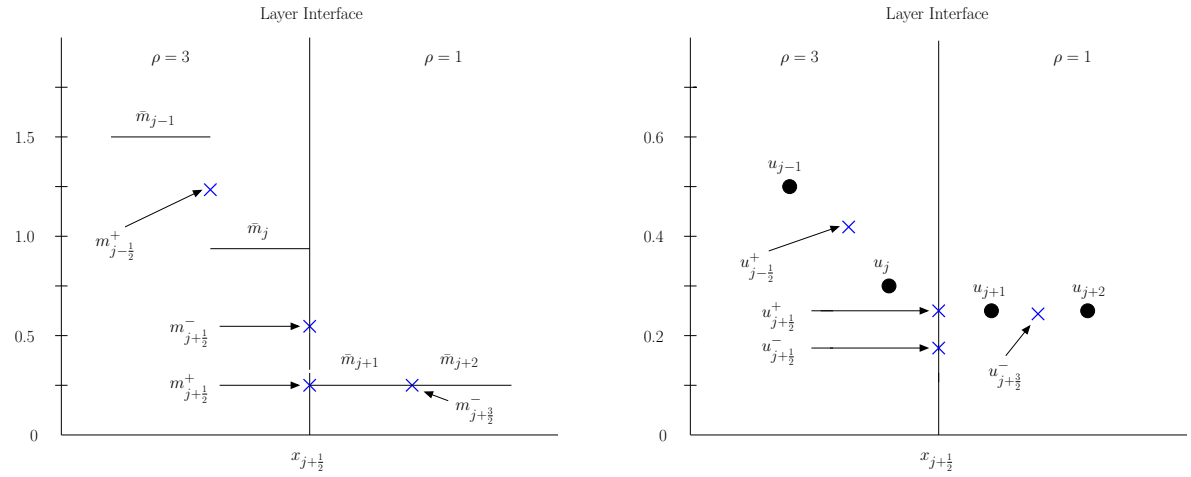

Figure 2.5: MinMod2 reconstruction applied to the cell averages of m (left) and the obtained point values of $u = m/\rho$ (right). Notice the oscillation in the u-field at $x = x_{j+\frac{1}{2}}$.

where $m = -\rho U\varepsilon$. The reconstructed point values are then

$$u^-_{j+\frac{1}{2}} = u^n_j + \frac{\Delta x}{2}(u_x)^n_j, \qquad u^+_{j+\frac{1}{2}} = u^n_{j+1} - \frac{\Delta x}{2}(u_x)^n_{j+1},$$
$$\sigma^-_{j+\frac{1}{2}} = \sigma^n_j + \frac{\Delta x}{2}(\sigma_x)^n_j, \qquad \sigma^+_{j+\frac{1}{2}} = \sigma^n_{j+1} - \frac{\Delta x}{2}(\sigma_x)^n_{j+1},$$

where the slopes are obtained using, for example, the generalized minmod limiter:

$$(u_x)^n_j = \text{minmod}\left(\theta\frac{u^n_{j+1} - u^n_j}{\Delta x}, \frac{u^n_{j+1} - u^n_{j-1}}{2\Delta x}, \theta\frac{u^n_j - u^n_{j-1}}{\Delta x}\right),$$
$$(\sigma_x)^n_j = \text{minmod}\left(\theta\frac{\sigma^n_{j+1} - \sigma^n_j}{\Delta x}, \frac{\sigma^n_{j+1} - \sigma^n_{j-1}}{2\Delta x}, \theta\frac{\sigma^n_j - \sigma^n_{j-1}}{\Delta x}\right).$$

We can now calculate the corresponding point values of ε, m, and U, which are also used in the calculation of the numerical fluxes. First, we introduce the notations $\rho^\pm_{j+\frac{1}{2}} := \rho(x_{j+\frac{1}{2}} \pm 0)$ and $K^\pm_{j+\frac{1}{2}} := K(x_{j+\frac{1}{2}} \pm 0)$, and compute $\varepsilon^\pm_{j+\frac{1}{2}}$ by

$$\varepsilon^\pm_{j+\frac{1}{2}} = \frac{-1 + \sqrt{1 + 4\beta\sigma^\pm_{j+\frac{1}{2}}}}{2\beta K^\pm_{j+\frac{1}{2}}} \quad \text{or} \quad \varepsilon^\pm_{j+\frac{1}{2}} = \frac{\ln(\sigma^\pm_{j+\frac{1}{2}} + 1)}{K^\pm_{j+\frac{1}{2}}}, \tag{2.18}$$

depending on which stress-strain relation, (1.4) or (1.5), is being used. Next, we compute $U^\pm_{j+\frac{1}{2}}$. To this end, we need to use the formula $U = -u/\varepsilon$, which becomes singular if $\varepsilon \approx 0$. We therefore desingularize this calculation by using the approach from [15]:

$$U^\pm_{j+\frac{1}{2}} = -\frac{\sqrt{2}\varepsilon^\pm_{j+\frac{1}{2}}u^\pm_{j+\frac{1}{2}}}{\sqrt{\left(\varepsilon^\pm_{j+\frac{1}{2}}\right)^4 + \max\left(\left(\varepsilon^\pm_{j+\frac{1}{2}}\right)^4, \delta\right)}},$$

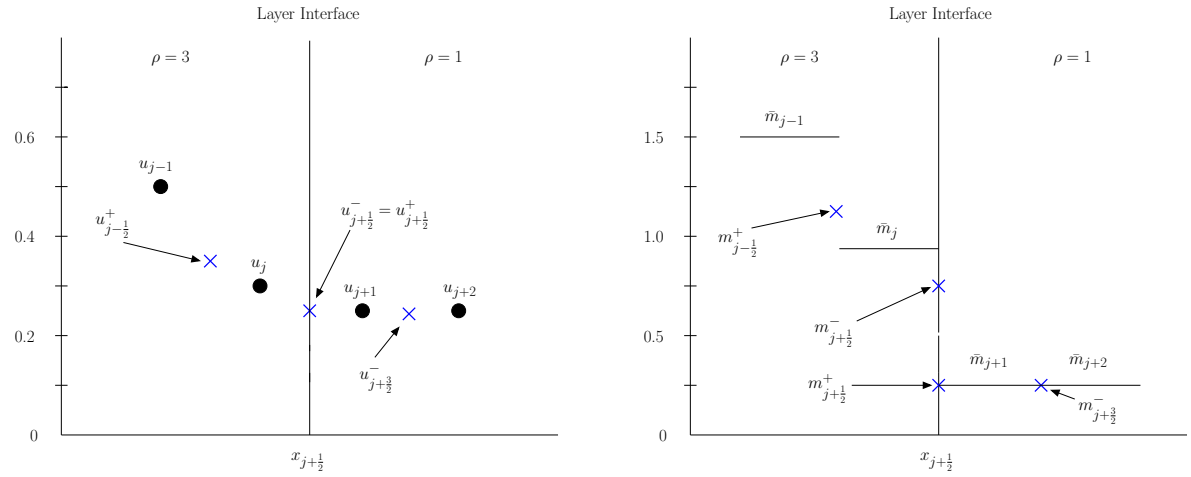

Figure 2.6: MinMod2 reconstruction applied to the point values of u (left) and the obtained point values of $m = \rho u$ (right). The resulting reconstruction is non-oscillatory.

where δ is taken to be a small positive number (in our numerical experiments, we have taken δ to be dependent on the size of the mesh in the following way: if $\Delta x = 2^{-p}$, $\delta = 2^{-24}(\Delta x)^4$. However, this selection of δ is not crucial at all and other values of δ can be successfully used). Finally, we obtain $m^{\pm}_{j+\frac{1}{2}} = -\rho^{\pm}_{j+\frac{1}{2}} U^{\pm}_{j+\frac{1}{2}} \varepsilon^{\pm}_{j+\frac{1}{2}}$.

2.2.2 Special Projection Step

We now turn to the description of the main novel part of our scheme – a special projection step which is crucial for the stability of the proposed method. The projection step in §2.1 involved the intermediate cell averages $\bar{\mathbf{q}}^{\text{int}}_j$, $\bar{\mathbf{q}}^{\text{int}}_{j+\frac{1}{2}}$, and the slopes $(\mathbf{q}_x)^{\text{int}}_{j+\frac{1}{2}}$, used to obtain a piecewise linear reconstruction (schematically shown in Figure 2.7 on the left), which is then averaged over the cell $(x_{j-\frac{1}{2}}, x_{j+\frac{1}{2}})$. Unfortunately, this leads to oscillations in the continuous fields (u and σ).

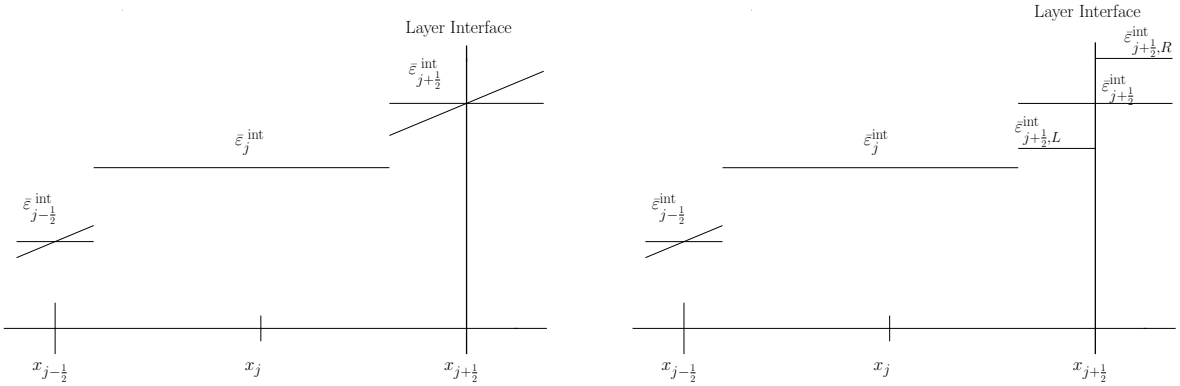

Figure 2.7: Piecewise linear reconstruction of the first component of $\bar{\mathbf{q}}^{\text{int}}$ using the minmod reconstruction as in §2.1 (left) and the modified approach (right).

The main reason the instabilities develop is averaging of conservative quantities (ε and m) across the layer interfaces where both ρ and K jump. Let us assume that the layer interface is located at $x = x_{j+\frac{1}{2}}$. Then, the averaged quantities $\bar{\mathbf{q}}^{\text{int}}_{j+\frac{1}{2}}$ are very inaccurate and thus they are to be replaced at the projection step with two constant pieces $\bar{\mathbf{q}}^{\text{int}}_{j+\frac{1}{2},L}$ and $\bar{\mathbf{q}}^{\text{int}}_{j+\frac{1}{2},R}$, see Figure 2.7 (right). Their values are determined using the following two requirements. First, from the conservation of ε and m, we have

$$\frac{1}{2}\left(\bar{\mathbf{q}}^{\text{int}}_{j+\frac{1}{2},L}+\bar{\mathbf{q}}^{\text{int}}_{j+\frac{1}{2},R}\right)=\bar{\mathbf{q}}^{\text{int}}_{j+\frac{1}{2}}. \tag{2.19}$$

Second, we would like to make sure that σ and u are continuous across the layer interface. This requirement should be satisfied for both finite Δt and in the case when $\Delta t\to 0$ (i.e., if we pass to the semi-discrete limit when $\sigma^{\text{int}}_{j+\frac{1}{2},L}\to\sigma^{-}_{j+\frac{1}{2}}$ and $\sigma^{\text{int}}_{j+\frac{1}{2},R}\to\sigma^{+}_{j+\frac{1}{2}}$). Therefore, we take

$$\sigma^{\text{int}}_{j+\frac{1}{2},L}=\sigma^{\text{int}}_{j+\frac{1}{2},R},\qquad u^{\text{int}}_{j+\frac{1}{2},L}=u^{\text{int}}_{j+\frac{1}{2},R},$$

which can be rewritten in terms of the new conservative quantities $\bar{\mathbf{q}}^{\text{int}}_{j+\frac{1}{2},L}$ and $\bar{\mathbf{q}}^{\text{int}}_{j+\frac{1}{2},R}$ as follows:

$$K^{-}_{j+\frac{1}{2}}\bar{\varepsilon}^{\text{int}}_{j+\frac{1}{2},L}=K^{+}_{j+\frac{1}{2}}\bar{\varepsilon}^{\text{int}}_{j+\frac{1}{2},R},\qquad \frac{\bar{m}^{\text{int}}_{j+\frac{1}{2},L}}{\rho^{-}_{j+\frac{1}{2}}}=\frac{\bar{m}^{\text{int}}_{j+\frac{1}{2},R}}{\rho^{+}_{j+\frac{1}{2}}}. \tag{2.20}$$

After solving the linear system (2.19), (2.20), we obtain

$$\bar{\mathbf{q}}^{\text{int}}_{j+\frac{1}{2},L}=\begin{pmatrix}\bar{\varepsilon}^{\text{int}}_{j+\frac{1}{2},L}\\ \bar{m}^{\text{int}}_{j+\frac{1}{2},L}\end{pmatrix}=\begin{pmatrix}\dfrac{2K^{+}_{j+\frac{1}{2}}}{K^{-}_{j+\frac{1}{2}}+K^{+}_{j+\frac{1}{2}}}\bar{\varepsilon}^{\text{int}}_{j+\frac{1}{2}}\\ \dfrac{2\rho^{-}_{j+\frac{1}{2}}}{\rho^{-}_{j+\frac{1}{2}}+\rho^{+}_{j+\frac{1}{2}}}\bar{m}^{\text{int}}_{j+\frac{1}{2}}\end{pmatrix},$$

$$\bar{\mathbf{q}}^{\text{int}}_{j+\frac{1}{2},R}=\begin{pmatrix}\bar{\varepsilon}^{\text{int}}_{j+\frac{1}{2},R}\\ \bar{m}^{\text{int}}_{j+\frac{1}{2},R}\end{pmatrix}=\begin{pmatrix}\dfrac{2K^{-}_{j+\frac{1}{2}}}{K^{-}_{j+\frac{1}{2}}+K^{+}_{j+\frac{1}{2}}}\bar{\varepsilon}^{\text{int}}_{j+\frac{1}{2}}\\ \dfrac{2\rho^{+}_{j+\frac{1}{2}}}{\rho^{-}_{j+\frac{1}{2}}+\rho^{+}_{j+\frac{1}{2}}}\bar{m}^{\text{int}}_{j+\frac{1}{2}}\end{pmatrix}.$$

We now define the auxiliary diagonal matrices $\mathcal{A}^{+}_{j+\frac{1}{2}}$ and $\mathcal{A}^{-}_{j+\frac{1}{2}}$,

$$\mathcal{A}^{+}_{j+\frac{1}{2}}:=\begin{pmatrix}\dfrac{2K^{-}_{j+\frac{1}{2}}}{K^{-}_{j+\frac{1}{2}}+K^{+}_{j+\frac{1}{2}}} & 0\\ 0 & \dfrac{2\rho^{+}_{j+\frac{1}{2}}}{\rho^{-}_{j+\frac{1}{2}}+\rho^{+}_{j+\frac{1}{2}}}\end{pmatrix},\quad \mathcal{A}^{-}_{j+\frac{1}{2}}:=\begin{pmatrix}\dfrac{2K^{+}_{j+\frac{1}{2}}}{K^{-}_{j+\frac{1}{2}}+K^{+}_{j+\frac{1}{2}}} & 0\\ 0 & \dfrac{2\rho^{-}_{j+\frac{1}{2}}}{\rho^{-}_{j+\frac{1}{2}}+\rho^{+}_{j+\frac{1}{2}}}\end{pmatrix}, \tag{2.21}$$

so that

$$\bar{\mathbf{q}}^{\text{int}}_{j+\frac{1}{2},L}=\mathcal{A}^{-}_{j+\frac{1}{2}}\bar{\mathbf{q}}^{\text{int}}_{j+\frac{1}{2}},\qquad \bar{\mathbf{q}}^{\text{int}}_{j+\frac{1}{2},R}=\mathcal{A}^{+}_{j+\frac{1}{2}}\bar{\mathbf{q}}^{\text{int}}_{j+\frac{1}{2}}. \tag{2.22}$$

Note that if there is no layer interface at $x_{j+\frac12}$, then $K^-_{j+\frac12}=K^+_{j+\frac12}$ and $\rho^-_{j+\frac12}=\rho^+_{j+\frac12}$ so that $\mathcal{A}^-_{j+\frac12}=\mathcal{A}^+_{j+\frac12}=I$ and $\bar{\mathbf{q}}^{\rm int}_{j+\frac12,L}=\bar{\mathbf{q}}^{\rm int}_{j+\frac12,R}=\bar{\mathbf{q}}^{\rm int}_{j+\frac12}$.

After modifying the reconstruction $\widetilde{\mathbf{q}}^{\rm int}$, we are now ready to perform the projection step which will be different from (2.9) in the cells next to the layer interface. Without loss of generality, we assume that the interface is located on the right and obtain (compare with (2.9)):

$$\bar{\mathbf{q}}^{n+1}_j=\frac{1}{\Delta x}\int\limits_{x_{j-\frac12}}^{x_{j+\frac12}}\widetilde{\mathbf{q}}^{\rm int}(\xi)\,d\xi=\lambda a_{j-\frac12}\bar{\mathbf{q}}^{\rm int}_{j-\frac12}+\left[1-\lambda\left(a_{j-\frac12}+a_{j+\frac12}\right)\right]\bar{\mathbf{q}}^{\rm int}_j+\lambda a_{j+\frac12}\bar{\mathbf{q}}^{\rm int}_{j+\frac12,L}$$
$$+\frac{\Delta x}{2}\left(\lambda a_{j-\frac12}\right)^2(\mathbf{q}_x)^{n+1}_{j-\frac12}. \tag{2.23}$$

We then substitute (2.7), (2.8), (2.21) and (2.22) into (2.23), subtract $\bar{\mathbf{q}}^n_j$ from both sides, divide by Δt, and take into account that $\mathcal{A}^-_{j-\frac12}=\mathcal{A}^+_{j-\frac12}=I$ (and hence $\bar{\mathbf{q}}^{\rm int}_{j-\frac12}=\bar{\mathbf{q}}^{\rm int}_{j-\frac12,R}$) to obtain

$$\begin{aligned}
\frac{\bar{\mathbf{q}}^{n+1}_j-\bar{\mathbf{q}}^n_j}{\Delta t}&=\frac{a_{j-\frac12}}{\Delta x}\bar{\mathbf{q}}^{\rm int}_{j-\frac12,R}+\left[\frac{1}{\Delta t}-\frac{a_{j-\frac12}+a_{j+\frac12}}{\Delta x}\right]\bar{\mathbf{q}}^{\rm int}_{j+\frac12}+\frac{a_{j+\frac12}}{\Delta x}\bar{\mathbf{q}}^{\rm int}_{j+\frac12,L}-\frac{\bar{\mathbf{q}}^n_j}{\Delta t}+\frac{\lambda}{2}a^2_{j-\frac12}(\mathbf{q}_x)^{n+1}_{j-\frac12}\\
&=\frac{a_{j-\frac12}}{\Delta x}\mathcal{A}^+_{j-\frac12}\bar{\mathbf{q}}^{\rm int}_{j-\frac12}+\left[\frac{1}{\Delta t}-\frac{a_{j-\frac12}+a_{j+\frac12}}{\Delta x}\right]\bar{\mathbf{q}}^{\rm int}_{j+\frac12}+\frac{a_{j+\frac12}}{\Delta x}\mathcal{A}^-_{j+\frac12}\bar{\mathbf{q}}^{\rm int}_{j+\frac12}-\frac{\bar{\mathbf{q}}^n_j}{\Delta t}+\frac{\lambda}{2}a^2_{j-\frac12}(\mathbf{q}_x)^{n+1}_{j-\frac12}\\
&=\frac{a_{j-\frac12}}{2\Delta x}\mathcal{A}^+_{j-\frac12}\left(\bar{\mathbf{q}}^n_{j-1}+\bar{\mathbf{q}}^n_j\right)-\frac{\mathcal{A}^+_{j-\frac12}}{2\Delta x}\left[\mathbf{f}\left(\mathbf{C}\big(x^n_{j-\frac12,r}\big);\mathbf{q}^{n+\frac12}_{j-\frac12,r}\right)-\mathbf{f}\left(\mathbf{C}\big(x^n_{j-\frac12,\ell}\big);\mathbf{q}^{n+\frac12}_{j-\frac12,\ell}\right)\right]\\
&\quad-\frac{(a_{j-\frac12}+a_{j+\frac12})}{\Delta x}\bar{\mathbf{q}}^n_j-\frac{1}{\Delta x}\left[\mathbf{f}\left(\mathbf{C}\big(x^n_{j+\frac12,\ell}\big);\mathbf{q}^{n+\frac12}_{j+\frac12,\ell}\right)-\mathbf{f}\left(\mathbf{C}\big(x^n_{j-\frac12,r}\big);\mathbf{q}^{n+\frac12}_{j-\frac12,r}\right)\right]+\frac{\lambda}{2}a^2_{j-\frac12}(\mathbf{q}_x)^{n+1}_{j-\frac12}\\
&\quad+\frac{a_{j+\frac12}}{2\Delta x}\mathcal{A}^-_{j+\frac12}\left(\bar{\mathbf{q}}^n_j+\bar{\mathbf{q}}^n_{j+1}\right)-\frac{\mathcal{A}^-_{j+\frac12}}{2\Delta x}\left[\mathbf{f}\left(\mathbf{C}\big(x^n_{j+\frac12,r}\big);\mathbf{q}^{n+\frac12}_{j+\frac12,r}\right)-\mathbf{f}\left(\mathbf{C}\big(x^n_{j+\frac12,\ell}\big);\mathbf{q}^{n+\frac12}_{j+\frac12,\ell}\right)\right]\\
&=-\frac{1}{2\Delta x}\Big\{\mathcal{A}^-_{j+\frac12}\mathbf{f}\left(\mathbf{C}\big(x^n_{j+\frac12,r}\big);\mathbf{q}^{n+\frac12}_{j+\frac12,r}\right)+\left(2I-\mathcal{A}^-_{j+\frac12}\right)\mathbf{f}\left(\mathbf{C}\big(x^n_{j+\frac12,\ell}\big);\mathbf{q}^{n+\frac12}_{j+\frac12,\ell}\right)\\
&\qquad-\left[\left(2I-\mathcal{A}^+_{j-\frac12}\right)\mathbf{f}\left(\mathbf{C}\big(x^n_{j-\frac12,r}\big);\mathbf{q}^{n+\frac12}_{j-\frac12,r}\right)+\mathcal{A}^+_{j-\frac12}\mathbf{f}\left(\mathbf{C}\big(x^n_{j-\frac12,\ell}\big);\mathbf{q}^{n+\frac12}_{j-\frac12,\ell}\right)\right]\Big\}\\
&\quad+a_{j+\frac12}\left(\mathcal{A}^-_{j+\frac12}\bar{\mathbf{q}}^n_{j+1}-\left(2I-\mathcal{A}^-_{j+\frac12}\right)\bar{\mathbf{q}}^n_j\right)-a_{j-\frac12}\left(\left(2I-\mathcal{A}^+_{j-\frac12}\right)\bar{\mathbf{q}}^n_j-\mathcal{A}^+_{j-\frac12}\bar{\mathbf{q}}^n_{j-1}\right)\\
&\quad+\frac{\lambda}{2}a^2_{j-\frac12}\left(\mathbf{q}_x\right)^{n+1}_{j-\frac12}.
\end{aligned}$$

Finally, sending $\Delta t\to0$ and using the fact that, according to (2.21), $\mathcal{A}^+_{j+\frac12}+\mathcal{A}^-_{j+\frac12}\equiv2I$, we arrive at the following semi-discretization:

$$\frac{d}{dt}\bar{\mathbf{q}}_j(t)=-\frac{\mathcal{A}^-_{j+\frac12}\mathbf{f}(\mathbf{C}^+_{j+\frac12};\mathbf{q}^+_{j+\frac12})+\mathcal{A}^+_{j+\frac12}\mathbf{f}(\mathbf{C}^-_{j+\frac12};\mathbf{q}^-_{j+\frac12})}{2\Delta x}$$

$$+\frac{\mathcal{A}^-_{j-\frac12}\mathbf{f}(\mathbf{C}^+_{j-\frac12};\mathbf{q}^+_{j-\frac12})+\mathcal{A}^+_{j-\frac12}\mathbf{f}(\mathbf{C}^-_{j-\frac12};\mathbf{q}^-_{j-\frac12})}{2\Delta x}$$

$$-\frac{1}{2\Delta x}\left[a_{j+\frac12}\left(\mathcal{A}^-_{j+\frac12}\mathbf{q}^+_{j+\frac12}-\mathcal{A}^+_{j+\frac12}\mathbf{q}^-_{j+\frac12}\right)-a_{j-\frac12}\left(\mathcal{A}^-_{j-\frac12}\mathbf{q}^+_{j-\frac12}-\mathcal{A}^+_{j-\frac12}\mathbf{q}^-_{j-\frac12}\right)\right]-\frac{a^2_{j-\frac12}}{2\Delta x}\mathbf{d}_{j-\frac12},$$

where $\mathbf{d}_{j-\frac12}$ is the same as in (2.13), (2.14).

The new semi-discrete central-upwind scheme can be then written in the flux form:

$$\frac{d}{dt}\bar{\mathbf{q}}_j(t)=-\frac{\mathbf{H}_{j+\frac12}(t)-\mathbf{H}_{j-\frac12}(t)}{\Delta x},\tag{2.24}$$

where the numerical fluxes are

$$\begin{aligned}\mathbf{H}_{j+\frac12}(t)=&\frac{\mathcal{A}^-_{j+\frac12}\mathbf{f}(\mathbf{C}^+_{j+\frac12};\mathbf{q}^+_{j+\frac12})+\mathcal{A}^+_{j+\frac12}\mathbf{f}(\mathbf{C}^-_{j-\frac12};\mathbf{q}^-_{j+\frac12})}{2}\\&-a_{j+\frac12}\left[\left(\mathcal{A}^-_{j+\frac12}\mathbf{q}^+_{j+\frac12}-\mathcal{A}^+_{j+\frac12}\mathbf{q}^-_{j+\frac12}\right)-\mathbf{d}_{j+\frac12}\right].\end{aligned}\tag{2.25}$$

The new numerical fluxes are similar to (2.12), except with the new $\mathcal{A}$ factors and the fact that the built-in "anti-diffusion" term $\mathbf{d}_{j+\frac12}$ is zero at material interfaces, i.e.,

$$\mathbf{d}_{j+\frac12}=\begin{cases}\text{minmod}\left(\mathbf{q}^+_{j+\frac12}-\mathbf{q}^*_{j+\frac12},\mathbf{q}^*_{j+\frac12}-\mathbf{q}^-_{j+\frac12}\right), & \text{if } \rho^-_{j+\frac12}=\rho^+_{j+\frac12},\\ 0, & \text{if } \rho^-_{j+\frac12}\neq\rho^+_{j+\frac12},\end{cases}\tag{2.26}$$

where

$$\mathbf{q}^*_{j+\frac12}=\frac{\mathbf{q}^+_{j+\frac12}+\mathbf{q}^-_{j+\frac12}}{2}+\frac{\mathbf{f}(\mathbf{C}^+_{j+\frac12};\mathbf{q}^+_{j+\frac12})-\mathbf{f}(\mathbf{C}^-_{j+\frac12};\mathbf{q}^-_{j+\frac12})}{2a_{j+\frac12}}.\tag{2.27}$$

We would like to recall that away from layer interfaces, $\mathcal{A}_{j+\frac12}=I$ by (2.21). Thus, the new flux (2.25) coincides with the old one, (2.12), there.

Remark 2.2 It is easy to check that for each component

$$\mathbf{d}^{(i)}_{j+\frac12}=(1-\boldsymbol{\mu}^{(i)}_{j+\frac12})(\mathcal{A}^-_{j+\frac12}\mathbf{q}^+_{j+\frac12}-\mathcal{A}^+_{j+\frac12}\mathbf{q}^-_{j+\frac12})^{(i)},\quad i=1,2,$$

where $\boldsymbol{\mu}^{(i)}_{j+\frac12}$ is between 0 and $\frac12$ (this explains why we use the term built-in "anti-diffusion" for $\mathbf{d}_{j+\frac12}$). Then, for instance, the first component of the numerical flux can be written as

$$\mathbf{H}^{(1)}_{j+\frac12}(t)=\frac{K^+_{j+\frac12}(U\varepsilon)^+_{j+\frac12}+K^-_{j+\frac12}(U\varepsilon)^-_{j+\frac12}}{K^+_{j+\frac12}+K^-_{j+\frac12}}-\frac{a_{j+\frac12}(1-\boldsymbol{\mu}^{(1)}_{j+\frac12})}{K^+_{j+\frac12}+K^-_{j+\frac12}}\left(K^+_{j+\frac12}\varepsilon^+_{j+\frac12}-K^-_{j+\frac12}\varepsilon^-_{j+\frac12}\right),\tag{2.28}$$

where

$$\boldsymbol{\mu}^{(1)}_{j+\frac12}=\frac{\mathbf{d}^{(1)}_{j+\frac12}}{\frac{2K^+_{j+\frac12}}{K^-_{j+\frac12}+K^+_{j+\frac12}}\varepsilon^+_{j+\frac12}-\frac{2K^-_{j+\frac12}}{K^-_{j+\frac12}+K^+_{j+\frac12}}\varepsilon^-_{j+\frac12}}=\frac{K^+_{j+\frac12}+K^-_{j+\frac12}}{2}\cdot\frac{\mathbf{d}^{(1)}_{j+\frac12}}{K^+_{j+\frac12}\varepsilon^+_{j+\frac12}-K^-_{j+\frac12}\varepsilon^-_{j+\frac12}}$$

whenever $K^+_{j+\frac12}\varepsilon^+_{j+\frac12}\neq K^-_{j+\frac12}\varepsilon^-_{j+\frac12}$ (otherwise $\boldsymbol{\mu}^{(1)}_{j+\frac12}$ can be taken to be any number).

2.2.3 Positivity Preserving Scheme

The new central-upwind scheme presented in §2.2.1 and 2.2.2 will be non-oscillatory and may provide a rather satisfactory resolution of the solitary waves. However, it will not guarantee positivity of ε and σ, which are supposed to be nonnegative. To fix this problem, we proceed as follows. We first apply the forward Euler discretization to the first component of (2.24) and obtain

$$\bar{\varepsilon}_j^{n+1} = \bar{\varepsilon}_j^n - \lambda\left(\mathbf{H}^{(1)}_{j+\frac{1}{2}} - \mathbf{H}^{(1)}_{j-\frac{1}{2}}\right), \tag{2.29}$$

with the numerical flux given by (2.28). We then notice that:

(i) By our reconstruction procedure described in §2.2.1,

$$(U\varepsilon)^{\pm}_{j\pm\frac{1}{2}} = U^{\pm}_{j\pm\frac{1}{2}}\cdot\varepsilon^{\pm}_{j\pm\frac{1}{2}}; \tag{2.30}$$

(ii) By the Taylor expansion of the function $\varepsilon(\sigma)$,

$$\bar{\varepsilon}_j^n = \frac{\varepsilon^+_{j-\frac{1}{2}} + \varepsilon^-_{j+\frac{1}{2}}}{2} - \frac{(\Delta x)^2}{16}\left((\sigma_x)_j\right)^2\left[\varepsilon''(\sigma_j^1) + \varepsilon''(\sigma_j^2)\right], \tag{2.31}$$

where σ_j^1 and σ_j^2 are some intermediate values (one of them is between σ_j^n and σ_{j-1}^n and the other is between σ_j^n and σ_{j+1}^n). Then, plugging (2.28), (2.30) and (2.31) into (2.29) results in

$$\begin{aligned}
\bar{\varepsilon}_j^{n+1} = {} & \left[\frac{1}{2} - \frac{\lambda K^+_{j-\frac{1}{2}}}{K^+_{j-\frac{1}{2}} + K^-_{j-\frac{1}{2}}}\left(a_{j-\frac{1}{2}}(1-\boldsymbol{\mu}^{(1)}_{j-\frac{1}{2}}) - U^+_{j-\frac{1}{2}}\right)\right]\varepsilon^+_{j-\frac{1}{2}} \\
& + \left[\frac{1}{2} - \frac{\lambda K^-_{j+\frac{1}{2}}}{K^+_{j+\frac{1}{2}} + K^-_{j+\frac{1}{2}}}\left(a_{j+\frac{1}{2}}(1-\boldsymbol{\mu}^{(1)}_{j+\frac{1}{2}}) + U^-_{j+\frac{1}{2}}\right)\right]\varepsilon^-_{j+\frac{1}{2}} \\
& + \frac{\lambda K^+_{j+\frac{1}{2}}}{K^+_{j+\frac{1}{2}} + K^-_{j+\frac{1}{2}}}\left(a_{j+\frac{1}{2}}(1-\boldsymbol{\mu}^{(1)}_{j+\frac{1}{2}}) - U^+_{j+\frac{1}{2}}\right)\varepsilon^+_{j+\frac{1}{2}} \\
& + \frac{\lambda K^-_{j-\frac{1}{2}}}{K^+_{j-\frac{1}{2}} + K^-_{j-\frac{1}{2}}}\left(a_{j-\frac{1}{2}}(1-\boldsymbol{\mu}^{(1)}_{j-\frac{1}{2}}) + U^-_{j-\frac{1}{2}}\right)\varepsilon^-_{j-\frac{1}{2}} - \frac{(\Delta x)^2}{16}\left((\sigma_x)_j\right)^2\left[\varepsilon''(\sigma_j^1) + \varepsilon''(\sigma_j^2)\right].
\end{aligned} \tag{2.32}$$

To show that $\bar{\varepsilon}_j^{n+1} \geq 0$, it will suffice to make sure that each term on the right hand side (RHS) of (2.32) is nonnegative. The last term is nonnegative since $\varepsilon(\sigma)$ is a concave down function, that is, $\varepsilon''(\sigma) < 0$ for all σ. To make the other terms positive, we modify the definition of the local speeds given in §2.1 and set

$$a_{j+\frac{1}{2}} = \max\left\{\sqrt{\frac{(d\sigma/d\varepsilon)^+_{j+\frac{1}{2}}}{\rho^+_{j+\frac{1}{2}}}}, \sqrt{\frac{(d\sigma/d\varepsilon)^-_{j+\frac{1}{2}}}{\rho^-_{j+\frac{1}{2}}}}, \frac{\left|U^+_{j+\frac{1}{2}}\right|}{1-\boldsymbol{\mu}^{(1)}_{j+\frac{1}{2}}}, \frac{\left|U^-_{j+\frac{1}{2}}\right|}{1-\boldsymbol{\mu}^{(1)}_{j+\frac{1}{2}}}\right\}. \tag{2.33}$$

where $(d\sigma/d\varepsilon)^{\pm}_{j+\frac{1}{2}}$ are obtained from either (2.4) or (2.5) by substituting $K^{\pm}_{j+\frac{1}{2}}$ and $\varepsilon^{\pm}_{j+\frac{1}{2}}$ there. This ensures that the third and fourth terms on the RHS of (2.32) are nonnegative. The positivity of the first two terms will be guaranteed under the following CFL condition:

$$\Delta t \leq \frac{\Delta x}{2a\gamma}, \quad a := \max_j\left\{a_{j+\frac{1}{2}}\right\}, \quad \gamma := \max_j\left\{\frac{2\max\left\{K^-_{j+\frac{1}{2}}, K^+_{j+\frac{1}{2}}\right\}}{K^-_{j+\frac{1}{2}} + K^+_{j+\frac{1}{2}}}\right\}. \tag{2.34}$$

We summarize the obtained results in the following theorem.

Theorem 2.1 *Let the system* (2.17) *with* (1.2), (1.3) *and either* (1.4) *or* (1.5) *be discretized by the new central-upwind scheme* (2.24)–(2.27), (2.33) *which uses the reconstructed procedure described in* §2.2.1. *Assume that the system of ODEs* (2.24) *is solved by the forward Euler method and that for all* j, $\bar{\varepsilon}_j^n \geq 0$. *Then, for all* j, $\bar{\varepsilon}_j^{n+1} \geq 0$, *provided that* Δt *satisfies the CFL condition* (2.34).

Remark 2.3 Theorem 2.1 is still valid if the forward Euler method is replaced with a higher-order SSP ODE solver since such solvers can be written as a convex combination of several forward Euler steps.

3 Two-Dimensional Central Upwind Scheme

We follow [10] and use a "dimension-by-dimension" approach in order to extend the 1-D system to the following (nonlinear) 2-D elasticity system

$$\begin{aligned} \varepsilon_t - u_x - v_y &= 0,\\ (\rho(x,y)u)_t - \sigma_x(K(x,y);\varepsilon) &= 0,\\ (\rho(x,y)v)_t - \sigma_y(K(x,y);\varepsilon) &= 0, \end{aligned} \tag{3.1}$$

where u and v are the x- and y-velocities, respectively. The system (3.1) can be written as

$$\mathbf{q}_t(\mathbf{x},t) + \nabla_{\mathbf{x}}\mathbf{f}(\mathbf{C}(\mathbf{x});\mathbf{q}) = \mathbf{0}, \tag{3.2}$$

where $\mathbf{x} = (x,y)^T$,

$$\mathbf{q} = \begin{pmatrix} \varepsilon \\ m_u \\ m_v \end{pmatrix}, \quad \mathbf{f}(\mathbf{C}(\mathbf{x});\mathbf{q}) = \begin{pmatrix} -m_u/\rho \\ -\sigma \\ 0 \end{pmatrix}, \quad \mathbf{g}(\mathbf{C}(\mathbf{x});\mathbf{q}) = \begin{pmatrix} -m_v/\rho \\ 0 \\ -\sigma \end{pmatrix}. \tag{3.3}$$

Here, $m_u = \rho u$ and $m_v = \rho v$ denote the corresponding momenta and σ is defined as in either (1.4) or (1.5).

This elasticity system is relevant when the layers of material are either vertical or horizontal. In this case, one can set up a Cartesian grid for which material interfaces align with the cell interfaces as, for instance, in Figure 4.6. In a general 2-D case, the elasticity system is more complicated (see, e.g., [18]).

We design a new central-upwind scheme for the system (3.2), (3.3) along the same lines as in §2.2. We first define new "dummy" variables $U = -\frac{u}{\varepsilon}$ and $V = -\frac{v}{\varepsilon}$ and rewrite (3.1) as

$$\begin{aligned} \varepsilon_t + (U\varepsilon)_x + (V\varepsilon)_y &= 0,\\ (\rho U\varepsilon)_t + \sigma_x &= 0,\\ (\rho V\varepsilon)_t + \sigma_y &= 0, \end{aligned} \tag{3.4}$$

where $m_u = -\rho U\varepsilon$ and $m_v = -\rho V\varepsilon$.

We consider a uniform grid with $x_j = j\Delta x$, $y_k = k\Delta x$ and $t^n = n\Delta t$ and assume that the cell averages at time t^n,

$$\bar{\mathbf{q}}^n_{j,k} \approx \frac{1}{\Delta x\Delta y}\int\limits_{x_{j-\frac{1}{2}}}^{x_{j+\frac{1}{2}}}\int\limits_{y_{k-\frac{1}{2}}}^{y_{k+\frac{1}{2}}} \mathbf{q}(x,y,t^n)\,dxdy,$$

are available.

At the reconstruction step, we again (as in §2.2.1) reconstruct the continuous flux variables instead of the discontinuous conservative ones. This means that the point values at the cell centers,

$$u^n_{j,k} = \frac{(\bar{m}_u)^n_{j,k}}{\rho_{j,k}}, \qquad v^n_{j,k} = \frac{(\bar{m}_v)^n_{j,k}}{\rho_{j,k}}, \qquad \sigma^n_{j,k} = K_{j,k}\bar{\varepsilon}^n_{j,k} + \beta K^2_{j,k}(\bar{\varepsilon}^n_{j,k})^2 \quad \text{or} \quad \sigma^n_{j,k} = e^{K_{j,k}\bar{\varepsilon}^n_{j,k}} - 1,$$

are used to obtain the reconstructed values at the corresponding sides of cell (j,k):

$$\begin{aligned}
&u^{\rm E}_{j,k} = u^n_{j,k} + \frac{\Delta x}{2}(u_x)^n_{j,k}, && u^{\rm N}_{j,k} = u^n_{j,k} + \frac{\Delta y}{2}(u_y)^n_{j,k},\\
&u^{\rm W}_{j,k} = u^n_{j,k} - \frac{\Delta x}{2}(u_x)^n_{j,k}, && u^{\rm S}_{j,k} = u^n_{j,k} - \frac{\Delta y}{2}(u_y)^n_{j,k},\\
&u^{\rm NE}_{j,k} = u^n_{j,k} + \frac{\Delta x}{2}(u_x)^n_{j,k} + \frac{\Delta y}{2}(u_y)^n_{j,k}, && u^{\rm NW}_{j,k} = u^n_{j,k} - \frac{\Delta x}{2}(u_x)^n_{j,k} + \frac{\Delta y}{2}(u_y)^n_{j,k},\\
&u^{\rm SE}_{j,k} = u^n_{j,k} + \frac{\Delta x}{2}(u_x)^n_{j,k} - \frac{\Delta y}{2}(u_y)^n_{j,k}, && u^{\rm SW}_{j,k} = u^n_{j,k} - \frac{\Delta x}{2}(u_x)^n_{j,k} - \frac{\Delta y}{2}(u_y)^n_{j,k}.
\end{aligned} \tag{3.5}$$

To ensure a non-oscillatory nature of the scheme, the slopes in (3.5), $(u_x)^n_{j,k}$ and $(u_y)^n_{j,k}$, are to be computed using (one's favorite) nonlinear limiter. In the numerical experiment reported in §4, we have used the MinMod2 limiter:

$$\begin{aligned}
(u_x)^n_{j,k} &= \text{minmod}\left(2\frac{u^n_{j+1,k}-u^n_{j,k}}{\Delta x}\,,\ \frac{u^n_{j+1,k}-u^n_{j-1,k}}{2\Delta x}\,,\ 2\frac{u^n_{j,k}-u^n_{j-1,k}}{\Delta x}\right),\\
(u_y)^n_{j,k} &= \text{minmod}\left(2\frac{u^n_{j,k+1}-u^n_{j,k}}{\Delta y}\,,\ \frac{u^n_{j,k+1}-u^n_{j,k-1}}{2\Delta y}\,,\ 2\frac{u^n_{j,k}-u^n_{j,k-1}}{\Delta y}\right).
\end{aligned}$$

The reconstructed values of the other two flux variables, v and σ, are obtained in a similar way.

We can now calculate the corresponding point values of ε, m_u, m_v, U and V. We first compute $\varepsilon^{\rm E}_{j,k}$, depending on which stress-strain relation is being used, by either

$$\varepsilon^{\rm E}_{j,k} = \frac{-1+\sqrt{1+4\beta\sigma^{\rm E}_{j,k}}}{2\beta K^{\rm E}_{j,k}} \quad \text{or} \quad \varepsilon^{\rm E}_{j,k} = \frac{\ln(\sigma^{\rm E}_{j,k}+1)}{K^{\rm E}_{j,k}}, \tag{3.6}$$

where $K^{\rm E}_{j,k} := K(x_{j+\frac{1}{2}}-0, y_k)$. To compute $U^{\rm E}_{j,k}$ and $V^{\rm E}_{j,k}$, we again desingularize the calculation by

$$U^{\rm E}_{j,k} = -\frac{\sqrt{2}\,\varepsilon^{\rm E}_{j,k}u^{\rm E}_{j,k}}{\sqrt{\left(\varepsilon^{\rm E}_{j,k}\right)^4 + \max\left\{\left(\varepsilon^{\rm E}_{j,k}\right)^4,\delta\right\}}} \quad \text{and} \quad V^{\rm E}_{j,k} = -\frac{\sqrt{2}\,\varepsilon^{\rm E}_{j,k}v^{\rm E}_{j,k}}{\sqrt{\left(\varepsilon^{\rm E}_{j,k}\right)^4 + \max\left\{\left(\varepsilon^{\rm E}_{j,k}\right)^4,\delta\right\}}},$$

where, as in the 1-D case, δ is taken to be a small positive number.

We finally obtain

$$(m_u)^E_{j,k} = -\rho^E_{j,k}U^E_{j,k}\varepsilon^E_{j,k} \quad \text{and} \quad (m_v)^E_{j,k} = -\rho^E_{j,k}V^E_{j,k}\varepsilon^E_{j,k}, \tag{3.7}$$

where $\rho^E_{j,k} := \rho(x_{j+\frac{1}{2}} - 0, y_k)$. All other point values of $\mathbf{q}$ along the boundary of cell (j,k) are calculated likewise.

As it was pointed out in [13, 14], a fully discrete 2-D scheme may be very cumbersome. Instead of working out its details, we directly proceed to the semi-discrete limit (along the lines of [13]) to obtain

$$\frac{d}{dt}\bar{\mathbf{q}}_{j,k}(t) = -\frac{\mathbf{H}^x_{j+\frac{1}{2},k}(t) - \mathbf{H}^x_{j-\frac{1}{2},k}(t)}{\Delta x} - \frac{\mathbf{H}^y_{j,k+\frac{1}{2}}(t) - \mathbf{H}^y_{j,k-\frac{1}{2}}(t)}{\Delta y}. \tag{3.8}$$

The numerical fluxes will be similar to those in [13], except that at material interfaces, the fluxes are modified in a similar fashion to §2.2.2. The new 2-D central-upwind fluxes are

$$\begin{aligned}
\mathbf{H}^x_{j+\frac{1}{2},k}(t) &= \frac{\mathcal{A}^{\mathrm{E}}_{j,k}\mathbf{f}(\mathbf{C}^{\mathrm{W}}_{j+1,k};\mathbf{q}^{\mathrm{W}}_{j+1,k}) + \mathcal{A}^{\mathrm{W}}_{j+1,k}\mathbf{f}(\mathbf{C}^{\mathrm{E}}_{j,k};\mathbf{q}^{\mathrm{E}}_{j,k})}{2} \\
&\quad -\frac{a^x_{j+\frac{1}{2},k}}{2}\left[\left(\mathcal{A}^{\mathrm{E}}_{j,k}\mathbf{q}^{\mathrm{W}}_{j+1,k} - \mathcal{A}^{\mathrm{W}}_{j+1,k}\mathbf{q}^{\mathrm{E}}_{j,k}\right) - \mathbf{d}^x_{j+\frac{1}{2},k}\right], \\
\mathbf{H}^y_{j,k+\frac{1}{2}}(t) &= \frac{\mathcal{A}^{\mathrm{N}}_{j,k}\mathbf{f}(\mathbf{C}^{\mathrm{S}}_{j,k+1};\mathbf{q}^{\mathrm{S}}_{j,k+1}) + \mathcal{A}^{\mathrm{S}}_{j,k+1}\mathbf{f}(\mathbf{C}^{\mathrm{N}}_{j,k};\mathbf{q}^{\mathrm{N}}_{j,k})}{2} \\
&\quad -\frac{a^y_{j,k+\frac{1}{2}}}{2}\left[\left(\mathcal{A}^{\mathrm{N}}_{j,k}\mathbf{q}^{\mathrm{S}}_{j,k+1} - \mathcal{A}^{\mathrm{S}}_{j,k+1}\mathbf{q}^{\mathrm{N}}_{j,k}\right) - \mathbf{d}^y_{j,k+\frac{1}{2}}\right].
\end{aligned} \tag{3.9}$$

The auxiliary diagonal matrices $\mathcal{A}$ in (3.9) are given by

$$\begin{aligned}
\mathcal{A}^{\mathrm{W}}_{j+1,k} &= \mathrm{diag}\left(\frac{2K^{\mathrm{E}}_{j,k}}{K^{\mathrm{E}}_{j,k} + K^{\mathrm{W}}_{j+1,k}}, \frac{2\rho^{\mathrm{W}}_{j+1,k}}{\rho^{\mathrm{E}}_{j,k} + \rho^{\mathrm{W}}_{j+1,k}}, 0\right), \\
\mathcal{A}^{\mathrm{E}}_{j,k} &= \mathrm{diag}\left(\frac{2K^{\mathrm{W}}_{j+1,k}}{K^{\mathrm{E}}_{j,k} + K^{\mathrm{W}}_{j+1,k}}, \frac{2\rho^{\mathrm{E}}_{j,k}}{\rho^{\mathrm{E}}_{j,k} + \rho^{\mathrm{W}}_{j+1,k}}, 0\right), \\
\mathcal{A}^{\mathrm{S}}_{j,k+1} &= \mathrm{diag}\left(\frac{2K^{\mathrm{N}}_{j,k}}{K^{\mathrm{N}}_{j,k} + K^{\mathrm{S}}_{j,k+1}}, 0, \frac{2\rho^{\mathrm{S}}_{j,k+1}}{\rho^{\mathrm{N}}_{j,k} + \rho^{\mathrm{S}}_{j,k+1}}\right), \\
\mathcal{A}^{\mathrm{N}}_{j,k} &= \mathrm{diag}\left(\frac{2K^{\mathrm{S}}_{j,k+1}}{K^{\mathrm{N}}_{j,k} + K^{\mathrm{S}}_{j,k+1}}, 0, \frac{2\rho^{\mathrm{N}}_{j,k}}{\rho^{\mathrm{N}}_{j,k} + \rho^{\mathrm{S}}_{j,k+1}}\right),
\end{aligned} \tag{3.10}$$

and as in the 1-D case, they will be equal to I away from a material interfaces. The local propagation speeds are estimated by

$$\begin{aligned}
a^x_{j+\frac{1}{2},k} &= \max\left\{\sqrt{\frac{(d\sigma/d\varepsilon)^{\mathrm{W}}_{j+1,k}}{\rho^{\mathrm{W}}_{j+1,k}}}, \sqrt{\frac{(d\sigma/d\varepsilon)^{\mathrm{E}}_{j,k}}{\rho^{\mathrm{E}}_{j,k}}}, \frac{U^{\mathrm{W}}_{j+1,k}}{1-\boldsymbol{\mu}^{(1)}_{j+\frac{1}{2},k}}, \frac{U^{\mathrm{E}}_{j,k}}{1-\boldsymbol{\mu}^{(1)}_{j+\frac{1}{2},k}}\right\}, \\
a^y_{j,k+\frac{1}{2}} &= \max\left\{\sqrt{\frac{(d\sigma/d\varepsilon)^{\mathrm{S}}_{j,k+1}}{\rho^{\mathrm{S}}_{j,k+1}}}, \sqrt{\frac{(d\sigma/d\varepsilon)^{\mathrm{N}}_{j,k}}{\rho^{\mathrm{N}}_{j,k}}}, \frac{V^{\mathrm{S}}_{j,k+1}}{1-\boldsymbol{\mu}^{(1)}_{j,k+\frac{1}{2}}}, \frac{V^{\mathrm{N}}_{j,k}}{1-\boldsymbol{\mu}^{(1)}_{j,k+\frac{1}{2}}}\right\}.
\end{aligned} \tag{3.11}$$

As in §2, $\mathbf{d}^x_{j+\frac12,k}$ and $\mathbf{d}^y_{j,k+\frac12}$ are built-in "anti-diffusion" terms from [13], which affect the numerical fluxes (3.9) away from layer interfaces:

$$\mathbf{d}^x_{j+\frac12,k}=\begin{cases}\mathcal{A}^x(\delta\mathbf{q})_{j+\frac12,k}, & \rho_{j,k}=\rho_{j+1,k},\\ 0, & \rho_{j,k}\neq\rho_{j+1,k},\end{cases}\qquad \mathbf{d}^y_{j,k+\frac12}=\begin{cases}\mathcal{A}^y(\delta\mathbf{q})_{j,k+\frac12}, & \rho_{j,k}=\rho_{j+1,k},\\ 0, & \rho_{j,k}\neq\rho_{j+1,k},\end{cases}\tag{3.12}$$

where

$$\begin{aligned}(\delta\mathbf{q})_{j+\frac12,k}&=\text{minmod}\left(\mathbf{q}^{\rm NW}_{j+1,k}-\mathbf{q}^*_{j+\frac12,k},\mathbf{q}^*_{j+\frac12,k}-\mathbf{q}^{\rm NE}_{j,k},\mathbf{q}^{\rm SW}_{j+1,k}-\mathbf{q}^*_{j+\frac12,k},\mathbf{q}^*_{j+\frac12,k}-\mathbf{q}^{\rm SE}_{j,k}\right),\\ (\delta\mathbf{q})_{j,k+\frac12}&=\text{minmod}\left(\mathbf{q}^{\rm SW}_{j,k+1}-\mathbf{q}^*_{j,k+\frac12},\mathbf{q}^*_{j,k+\frac12}-\mathbf{q}^{\rm NW}_{j,k},\mathbf{q}^{\rm SE}_{j,k+1}-\mathbf{q}^*_{j,k+\frac12},\mathbf{q}^*_{j,k+\frac12}-\mathbf{q}^{\rm NE}_{j,k}\right),\end{aligned}\tag{3.13}$$

the intermediate values of $\mathbf{q}$ are given by

$$\begin{aligned}\mathbf{q}^*_{j+\frac12,k}&=\frac{\mathbf{q}^{\rm W}_{j+1,k}+\mathbf{q}^{\rm E}_{j,k}}{2}-\frac{\mathbf{f}\left(\mathbf{C}^{\rm W}_{j+1,k};\mathbf{q}^{\rm W}_{j+1,k}\right)-\mathbf{f}\left(\mathbf{C}^{\rm E}_{j,k};\mathbf{q}^{\rm E}_{j,k}\right)}{2a^x_{j+\frac12,k}},\\ \mathbf{q}^*_{j,k+\frac12}&=\frac{\mathbf{q}^{\rm S}_{j,k+1}+\mathbf{q}^{\rm N}_{j,k}}{2}-\frac{\mathbf{g}\left(\mathbf{C}^{\rm S}_{j,k+1};\mathbf{q}^{\rm S}_{j,k+1}\right)-\mathbf{f}\left(\mathbf{C}^{\rm N}_{j,k};\mathbf{q}^{\rm N}_{j,k}\right)}{2a^y_{j,k+\frac12}},\end{aligned}\tag{3.14}$$

and the auxiliary diagonal matrices $\mathcal{A}^x$ and $\mathcal{A}^y$, needed to keep the third component of $\mathbf{H}^x_{j+\frac12,k}$ and the second component of $\mathbf{H}^y_{j,k+\frac12}$ to be zero, are simply equal to

$$\mathcal{A}^x=\text{diag}(1,1,0),\quad \mathcal{A}^y=\text{diag}(1,0,1).\tag{3.15}$$

As in the 1-D case, we define

$$\begin{aligned}\boldsymbol{\mu}^{(1)}_{j+\frac12,k}&=\frac{K^{\rm E}_{j,k}+K^{\rm W}_{j+1,k}}{2}\cdot\frac{\left(\mathbf{d}^x_{j+\frac12,k}\right)^{(1)}}{K^{\rm W}_{j+1,k}\varepsilon^{\rm W}_{j+1,k}-K^{\rm E}_{j,k}\varepsilon^{\rm E}_{j,k}},\\ \boldsymbol{\mu}^{(1)}_{j,k+\frac12}&=\frac{K^{\rm N}_{j,k}+K^{\rm S}_{j,k+1}}{2}\cdot\frac{\left(\mathbf{d}^y_{j,k+\frac12}\right)^{(1)}}{K^{\rm S}_{j,k+1}\varepsilon^{\rm S}_{j,k+1}-K^{\rm N}_{j,k}\varepsilon^{\rm N}_{j,k}},\end{aligned}$$

which have been used in (3.11). Hence, the first component of the numerical flux (3.9) can be rewritten as

$$\left(\mathbf{H}^x_{j+\frac12,k}\right)^{(1)}=\frac{K^{\rm E}_{j,k}(U\varepsilon)^{\rm E}_{j,k}+K^{\rm W}_{j+1,k}(U\varepsilon)^{\rm W}_{j+1,k}}{K^{\rm E}_{j,k}+K^{\rm W}_{j+1,k}}-\frac{a^x_{j+\frac12,k}\left(1-\boldsymbol{\mu}^{(1)}_{j+\frac12,k}\right)}{K^{\rm E}_{j,k}+K^{\rm W}_{j+1,k}}\left(K^{\rm W}_{j+1,k}\varepsilon^{\rm W}_{j+1,k}-K^{\rm E}_{j,k}\varepsilon^{\rm E}_{j,k}\right),\tag{3.16}$$

and

$$\left(\mathbf{H}^y_{j,k+\frac12}\right)^{(1)}=\frac{K^{\rm N}_{j,k}(V\varepsilon)^{\rm N}_{j,k}+K^{\rm S}_{j,k+1}(V\varepsilon)^{\rm S}_{j,k+1}}{K^{\rm N}_{j,k}+K^{\rm S}_{j,k+1}}-\frac{a^y_{j,k+\frac12}\left(1-\boldsymbol{\mu}^{(1)}_{j,k+\frac12}\right)}{K^{\rm N}_{j,k}+K^{\rm S}_{j,k+1}}\left(K^{\rm S}_{j,k+1}\varepsilon^{\rm S}_{j,k+1}-K^{\rm N}_{j,k}\varepsilon^{\rm N}_{j,k}\right).\tag{3.17}$$

3.1 Positivity Preserving Scheme

Theorem 3.1 *Consider the system* (3.4) *and the new central-upwind scheme* (3.8)–(3.15), (3.5)–(3.7). *Assume that the system of ODEs* (3.8) *is solved by the forward Euler method and that for all j,k,* $\bar{\varepsilon}^n_{j,k} \geq 0$. *Then, for all j,k,* $\bar{\varepsilon}^{n+1}_{j,k} \geq 0$, *provided that*

$$\Delta t \leq \min\left\{\frac{\Delta x}{4a\gamma_x}, \frac{\Delta y}{4b\gamma_y}\right\}, \tag{3.18}$$

where $a := \max\limits_{j,k}\left\{a^x_{j+\frac{1}{2},k}\right\}$, $b := \max\limits_{j,k}\left\{a^y_{j,k+\frac{1}{2}}\right\}$, $\gamma_x := \max\limits_{j,k}\left\{\dfrac{2\max\left\{K^{\rm E}_{j,k}, K^{\rm W}_{j+1,k}\right\}}{K^{\rm E}_{j,k}+K^{\rm W}_{j+1,k}}\right\}$, *and* $\gamma_y := \max\limits_{j,k}\left\{\dfrac{2\max\left\{K^{\rm N}_{j,k}, K^{\rm S}_{j,k+1}\right\}}{K^{\rm N}_{j,k}+K^{\rm S}_{j,k+1}}\right\}$.

Proof: The first component of (3.8) along with the forward Euler discretization in time can be written as

$$\bar{\varepsilon}^{n+1}_{j,k} = \bar{\varepsilon}^n_{j,k} - \lambda_x\left(\left(\mathbf{H}^x_{j+\frac{1}{2},k}\right)^{(1)} - \left(\mathbf{H}^x_{j-\frac{1}{2},k}\right)^{(1)}\right) - \lambda_y\left(\left(\mathbf{H}^y_{j,k+\frac{1}{2}}\right)^{(1)} - \left(\mathbf{H}^y_{j,k-\frac{1}{2}}\right)^{(1)}\right), \tag{3.19}$$

where $\lambda_x := \frac{\Delta t}{\Delta x}$ and $\lambda_y = \frac{\Delta t}{\Delta y}$. We now rewrite $\bar{\varepsilon}^{n+1}_{j,k}$ as a linear combination of the reconstructed point values of ε. To this end, we first use the Taylor expansion of the function $\varepsilon(\sigma)$ to obtain

$$\begin{aligned}\bar{\varepsilon}^n_{j,k} &= \frac{1}{4}\left(\varepsilon^{\rm E}_{j,k}+\varepsilon^{\rm W}_{j,k}+\varepsilon^{\rm S}_{j,k}+\varepsilon^{\rm N}_{j,k}\right)\\ &\quad - \frac{(\Delta x)^2}{16}\left((\sigma_x)_{j,k}\right)^2\left[\varepsilon''(\sigma^1_{j,k})+\varepsilon''(\sigma^2_{j,k})\right] - \frac{(\Delta y)^2}{16}\left((\sigma_y)_{j,k}\right)^2\left[\varepsilon''(\sigma^3_{j,k})+\varepsilon''(\sigma^4_{j,k})\right],\end{aligned} \tag{3.20}$$

where $\sigma^1_{j,k}, \sigma^2_{j,k}, \sigma^3_{j,k}$ and $\sigma^4_{j,k}$ are some intermediate values. We then notice that by our reconstruction procedure

$$(U\varepsilon)^{\rm E(W)}_{j,k} = U^{\rm E(W)}_{j,k}\cdot\varepsilon^{\rm E(W)}_{j,k}, \qquad (V\varepsilon)^{\rm N(S)}_{j,k} = V^{\rm N(S)}_{j,k}\cdot\varepsilon^{\rm N(S)}_{j,k}, \tag{3.21}$$

and plug (3.16), (3.17), (3.20) and (3.21) into (3.19) to end up with

$$\begin{aligned}\bar{\varepsilon}^{n+1}_{j,k} &= \left[\frac{1}{4} - \frac{\lambda_x K^{\rm W}_{j,k}}{K^{\rm E}_{j-1,k}+K^{\rm W}_{j,k}}\left(a^x_{j-\frac{1}{2},k}\left(1-\boldsymbol{\mu}^{(1)}_{j-\frac{1}{2},k}\right)-U^{\rm W}_{j,k}\right)\right]\varepsilon^{\rm W}_{j,k}\\ &\quad + \left[\frac{1}{4} - \frac{\lambda_x K^{\rm E}_{j,k}}{K^{\rm E}_{j,k}+K^{\rm W}_{j+1,k}}\left(a^x_{j+\frac{1}{2},k}\left(1-\boldsymbol{\mu}^{(1)}_{j+\frac{1}{2},k}\right)+U^{\rm E}_{j,k}\right)\right]\varepsilon^{\rm E}_{j,k}\\ &\quad + \frac{\lambda_x K^{\rm W}_{j+1,k}}{K^{\rm E}_{j,k}+K^{\rm W}_{j+1,k}}\left(a^x_{j+\frac{1}{2},k}\left(1-\boldsymbol{\mu}^{(1)}_{j+\frac{1}{2},k}\right)-U^{\rm W}_{j+1,k}\right)\varepsilon^{\rm W}_{j+1,k}\\ &\quad + \frac{\lambda_x K^{\rm E}_{j-1,k}}{K^{\rm E}_{j-1,k}+K^{\rm W}_{j,k}}\left(a^x_{j-\frac{1}{2},k}\left(1-\boldsymbol{\mu}^{(1)}_{j-\frac{1}{2},k}\right)+U^{\rm E}_{j-1,k}\right)\varepsilon^{\rm E}_{j-1,k}\\ &\quad + \left[\frac{1}{4} - \frac{\lambda_y K^{\rm S}_{j,k}}{K^{\rm N}_{j,k-1}+K^{\rm S}_{j,k}}\left(a^y_{j,k-\frac{1}{2}}\left(1-\boldsymbol{\mu}^{(1)}_{j,k-\frac{1}{2}}\right)-V^{\rm S}_{j,k}\right)\right]\varepsilon^{\rm S}_{j,k}\end{aligned}$$

$$
\begin{aligned}
&+\left[\frac{1}{4}-\frac{\lambda_y K^{\rm N}_{j,k}}{K^{\rm N}_{j,k}+K^{\rm S}_{j,k+1}}\left(a^y_{j,k+\frac12}\left(1-\boldsymbol{\mu}^{(1)}_{j,k+\frac12}\right)+V^{\rm N}_{j,k}\right)\right]\varepsilon^{\rm N}_{j,k}\\
&+\frac{\lambda_y K^{\rm S}_{j,k+1}}{K^{\rm N}_{j,k}+K^{\rm S}_{j,k+1}}\left(a^y_{j,k+\frac12}\left(1-\boldsymbol{\mu}^{(1)}_{j,k+\frac12}\right)-V^{\rm S}_{j,k+1}\right)\varepsilon^{\rm S}_{j,k+1}\\
&+\frac{\lambda_y K^{\rm N}_{j,k-1}}{K^{\rm N}_{j,k-1}+K^{\rm S}_{j,k}}\left(a^y_{j,k-\frac12}\left(1-\boldsymbol{\mu}^{(1)}_{j,k-\frac12}\right)+V^{\rm N}_{j,k-1}\right)\varepsilon^{\rm N}_{j,k-1}\\
&-\frac{(\Delta x)^2}{16}\Big(\big(\sigma_x\big)_{j,k}\Big)^2\left[\varepsilon''(\sigma^1_{j,k})+\varepsilon''(\sigma^2_{j,k})\right]-\frac{(\Delta y)^2}{16}\Big(\big(\sigma_y\big)_{j,k}\Big)^2\left[\varepsilon''(\sigma^3_{j,k})+\varepsilon''(\sigma^4_{j,k})\right]. \qquad (3.22)
\end{aligned}
$$

To show that $\bar{\varepsilon}^{n+1}_{j,k}\ge 0$, it will be enough to show that each term on the RHS of (3.22) is nonnegative. The last two terms are nonnegative since $\varepsilon(\sigma)$ is a concave down function. The third, fourth, seventh and eighth terms are guaranteed to be nonnegative by (3.11). Finally, the CFL condition (3.18) ensures that the remaining terms are also nonnegative. This completes the proof of the theorem. ■

Remark 3.1 Theorem 3.1 is still valid if the forward Euler method is replaced with a higher-order SSP ODE solver since such solvers can be written as a convex combination of several forward Euler steps.

4 Numerical Examples

4.1 One-Dimensional Example

We apply the scheme (2.24)–(2.27), (2.33), (2.34) with $\beta = 0.3$ to the system (1.1)–(1.4) in the example at which the original central-upwind scheme failed to produce accurate results (see §2.1). We take $\theta = 2$ for small time calculations ($t \le 240$) and $\theta = 1.6$ for large times ($t \ge 840$).

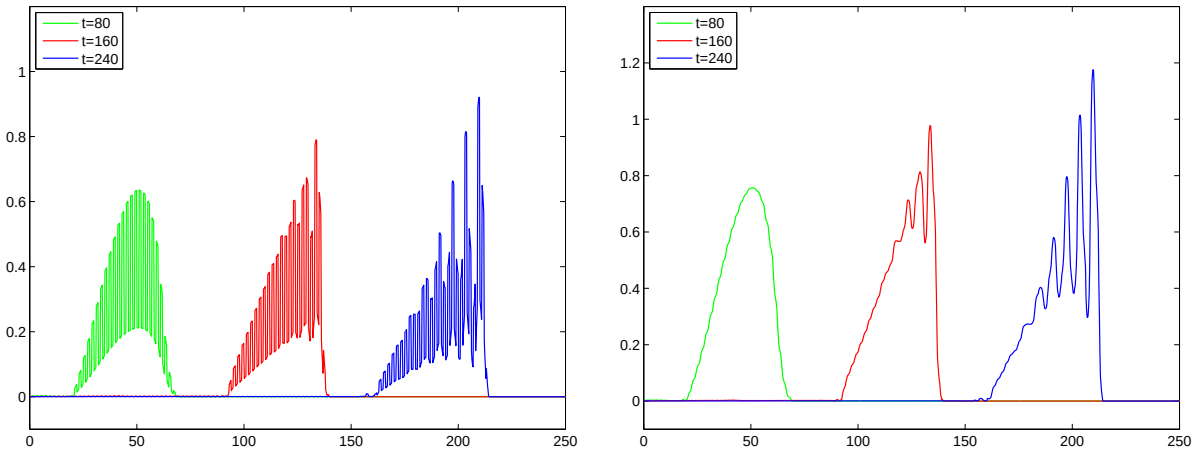

Figure 4.1: Nonlinear heterogeneous elasticity. Strain (left) and stress (right) at $t = 80, 160, 240$ with $\Delta x = 0.25$ (4 grid cells per layer of material) using the new central-upwind scheme.

In Figure 4.1, we plot the strain and stress at times $t = 80, 160, 240$ computed with $\Delta x = 0.25$, or 4 grid cells per layer of material. One can clearly observe the formation and initial stages of the evolution of the waves with dispersive behavior. These results are in good agreement with the results reported in [19] except that in our results both the strain and stress remain positive as guaranteed by Theorem 2.1. In Figure 4.2, we show the solution at time $t = 240$ from Figure 4.1, but zoomed in closer. We compare it with the reference solution, computed by our scheme with $\Delta x = 0.015625$, which is 64 grid cells per layer of material. We can see that at 4 cells per layer, we already achieve fairly good resolution (compare this with the results reported in Figure 2.3). We then double the number of cells per layer and present the obtained results in Figure 4.3. Both the strain and stress are now nicely captured and the resolution of contact waves across material interfaces is almost perfect.

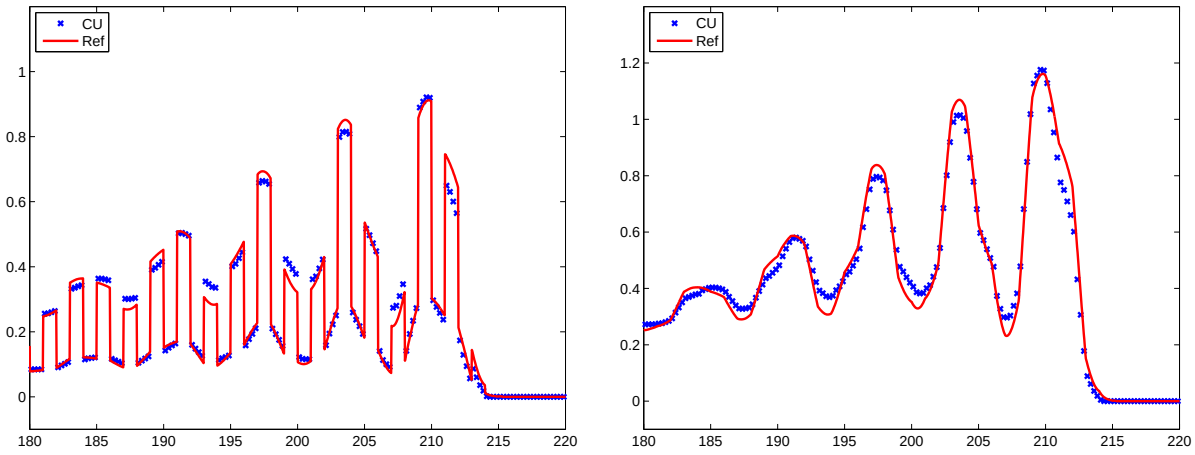

Figure 4.2: Nonlinear heterogeneous elasticity. Strain (left) and stress (right) at $t = 240$ with $\Delta x = 0.25$ (4 grid cells per layer of material) using the new central-upwind scheme. The reference solution was computed with $\Delta x = 0.03125$ (32 grid cells per layer of material).

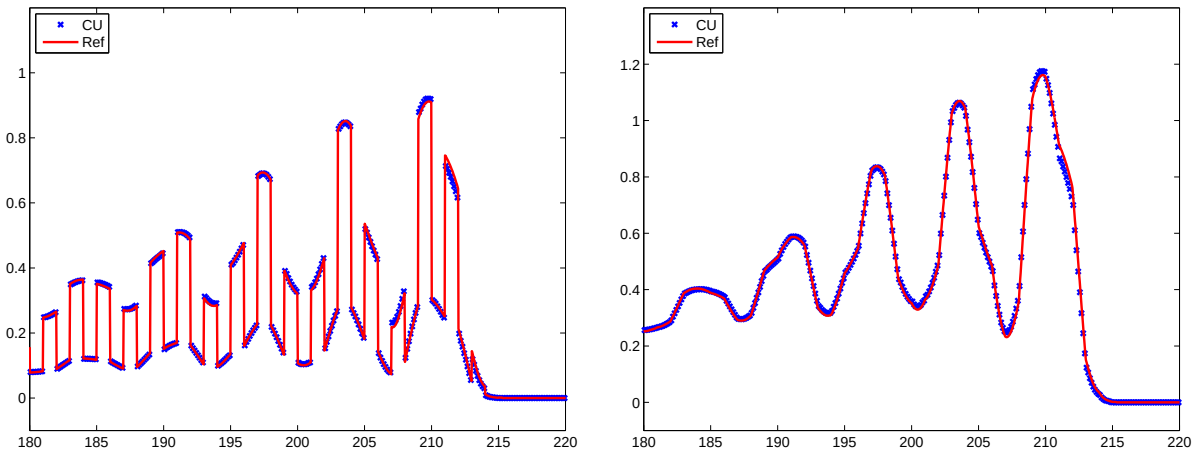

Figure 4.3: Same as in Figure 4.2 but with $\Delta x = 0.125$ (8 grid cells per layer of material) for the computed solution.

We now run the code for large times (up to $t = 2850$). The obtained results are shown

in Figure 4.4. At time $t = 60$, the boundary conditions are switched to the periodic ones. The oscillations in the shock wave shown in Figure 4.1 cause the heights of the waves to fluctuate which will result in the original wave to break up into solitary waves and propagate at different speeds. At time $t = 840$ our results do still agree with those reported in [19]. However, for larger times ($t = 1500$ and 2850), the height of the solitary waves computed by the central-upwind schemes are larger and thus they travel faster. This occurs thanks to smaller amount of numerical diffusion present at our scheme so that the solitary waves are not numerically damped as much as in [19]. In Figure 4.5, we show details of two peaks of the computed solitary wave at time $t = 2850$. One can clearly see that the contact waves are still sharply resolved and that the solution remains positive.

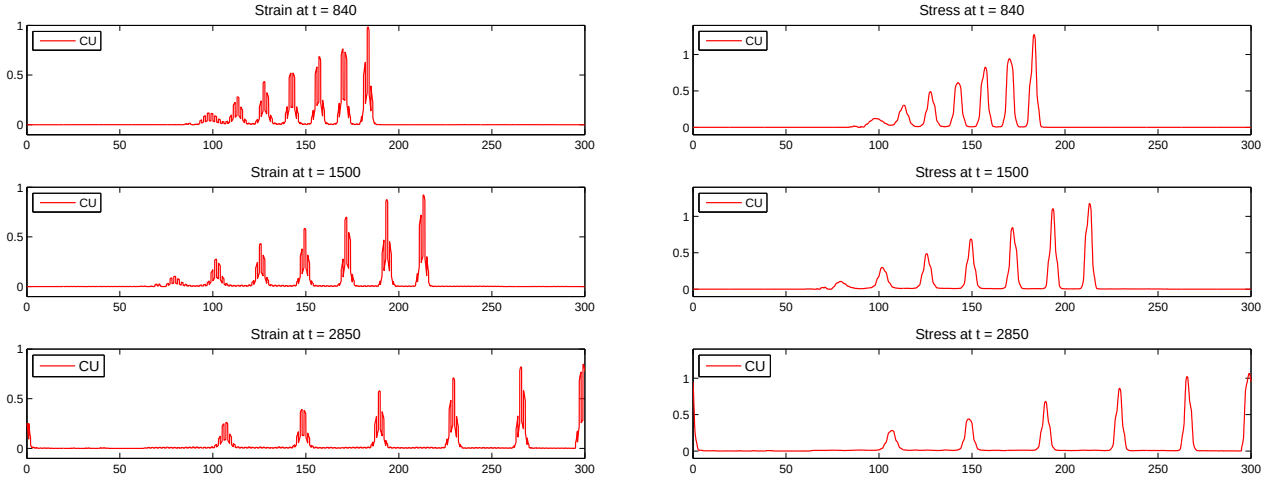

Figure 4.4: Strain (left) and stress (right) at times $t = 840, 1500, 2850$ with $\Delta x = 0.0625$ (16 grid cells per layer of material).

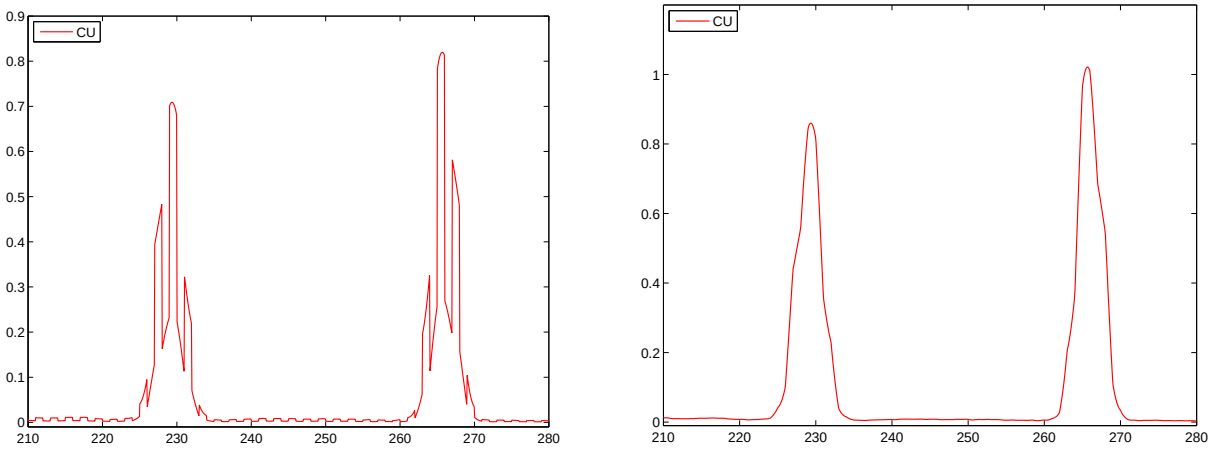

Figure 4.5: Strain (left) and stress (right) at time $t = 2850$ zoomed in with $\Delta x = 0.0625$ (16 grid cells per layer of material).

4.2 Two-Dimensional Example

Finally, we consider a 2-D numerical example. We use the problem setting from [10]: we use the stress-strain relation (1.5) and consider the domain $[0,100]\times[0,10]$ with alternating vertical material strips of length 1 (as outlined in Figure 4.6) so that, for all integer $j\geq 0$,

$$\rho(x,y)=\begin{cases}4, & \text{if } 2j<x<2j+1,\\ 1, & \text{otherwise,}\end{cases}\qquad K(x,y)=\begin{cases}4, & \text{if } 2j<x<2j+1,\\ 1, & \text{otherwise.}\end{cases}$$

The initial condition is a half of a Gaussian,

$$\sigma(x,y,0)=5e^{\frac{-x^2+(y-5)^2}{25}},\quad x>0,$$

with $u(x,y,0)\equiv v(x,y,0)\equiv 0$. The boundary conditions are periodic in the y-direction and reflexive in the x-direction.

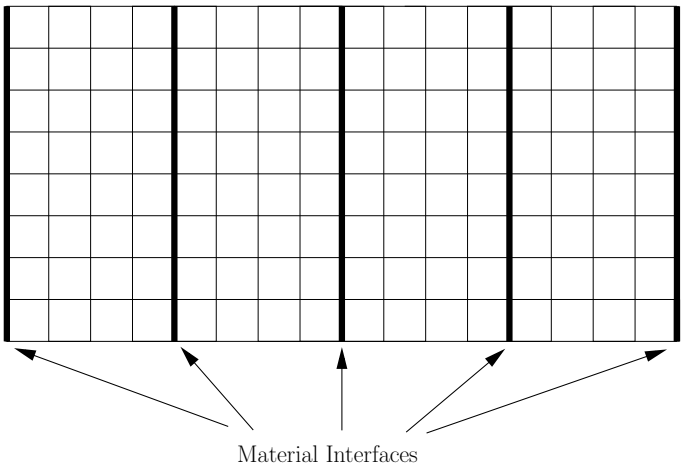

Figure 4.6: Layout of materials and a sample of adjusted Cartesian grid in two dimensions.

As one can see in Figures 4.7 and 4.8, by time $t=75$, the waves have started to evolve into solitary waves while remaining positive. One can also see that while the strain develops contact discontinuities (see Figure 4.7), the stress remains continuous (see Figure 4.8). Figures 4.9 and 4.10 show a 1-D slice along the line $y=5$ of the strain and stress, respectively. As one can see, the strain and stress behave in a similar fashion to the 1-D case. The oscillations in the shock wave for the strain will cause the heights of the wave to fluctuate which results in the different parts of the wave traveling at different speeds. The resolution achieved by the new central-upwind scheme is quite spectacular given that only 4 cells in the x-direction per a vertical layer of material have been used (in the presented calculations $\Delta x=\Delta y=0.25$). As in the 1-D case, no oscillations across material interfaces have been observed and no negative values have been produced as guaranteed by Theorem 3.1.

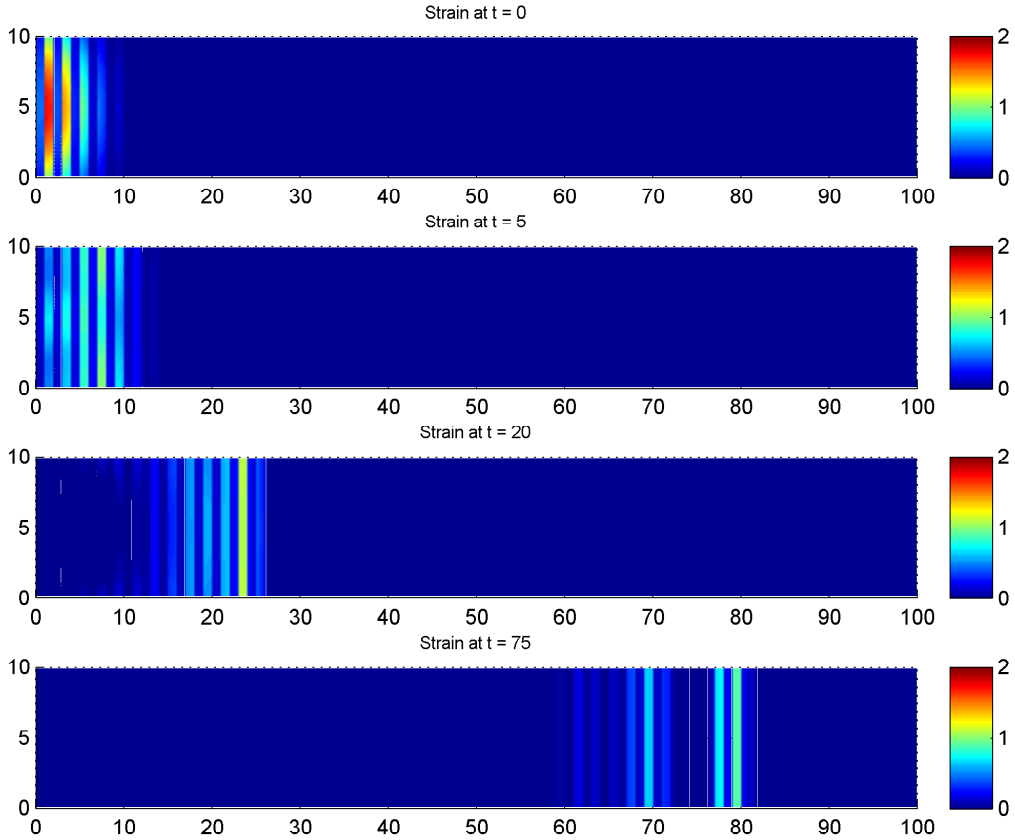

Figure 4.7: 2-D example. Strain at $t = 0, 5, 20, 75$ with $\Delta x = \Delta y = 0.25$.

References

[1] P. ARMINJON, M.-C. VIALLON, AND A. MADRANE, *A finite volume extension of the Lax-Friedrichs and Nessyahu-Tadmor schemes for conservation laws on unstructured grids*, Int. J. Comput. Fluid Dyn., 9 (1997), pp. 1–22.

[2] M. BEN-ARTZI AND J. FALCOVITZ, *Generalized Riemann problems in computational fluid dynamics*, vol. 11 of Cambridge Monographs on Applied and Computational Mathematics, Cambridge University Press, Cambridge, 2003.

[3] F. BIANCO, G. PUPPO, AND G. RUSSO, *High order central schemes for hyperbolic systems of conservation laws*, SIAM J. Sci. Comput, 21 (1999), pp. 294–322.

[4] E. GODLEWSKI AND P.-A. RAVIART, *Numerical approximation of hyperbolic systems of conservation laws*, vol. 118 of Applied Mathematical Sciences, Springer-Verlag, New York, 1996.

[5] S.K. GODUNOV, *A difference method for numerical calculation of discontinuous solutions of the equations of hydrodynamics*, Mat. Sb. (N.S.), 47 (89) (1959), pp. 271–306.

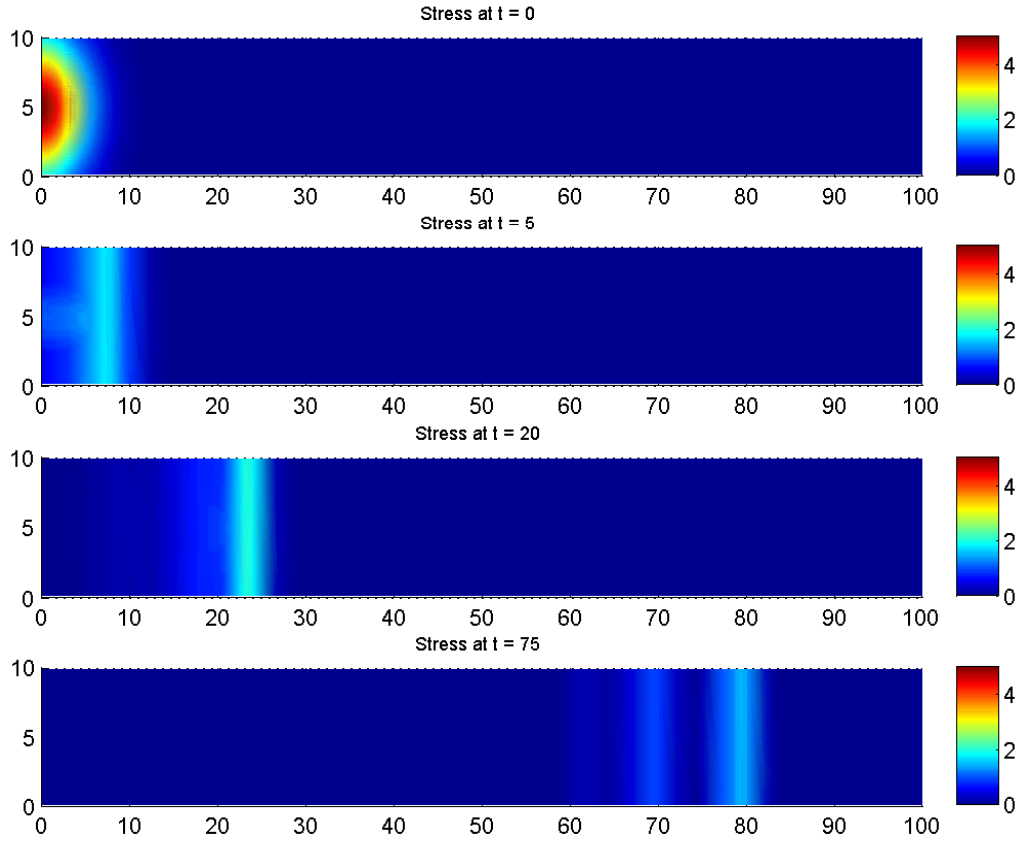

Figure 4.8: 2-D example. Stress at $t = 0, 5, 20, 75$ with $\Delta x = \Delta y = 0.25$.

[6] S. GOTTLIEB, C.W. SHU, AND E. TADMOR, *Strong stability-preserving high order time discretization methods*, SIAM Rev., 43 (2001), pp. 89–112.

[7] A. HARTEN, B. ENGQUIST, S. OSHER, AND S.R. CHAKRAVARTHY, *Uniformly high-order accurate essentially nonoscillatory schemes. III*, J. Comput. Phys., 71 (1987), pp. 231–303.

[8] A. HARTEN AND S. OSHER, *Uniformly high-order accurate nonoscillatory schemes. I*, SIAM J. Numer. Anal., 24 (1987), pp. 279–309.

[9] G.-S. JIANG AND E. TADMOR, *Nonoscillatory central schemes for multidimensional hyperbolic conservation laws*, SIAM J. Sci. Comput., 19 (1998), pp. 1892–1917 (electronic).

[10] D.I. KETCHESON, *High order strong stability preserving time integrators and numerical wave propagation methods for hyperbolic PDEs*, PhD dissertation, University of Washington, 2009.

[11] D. KRÖNER, *Numerical schemes for conservation laws*, Wiley-Teubner Series Advances in Numerical Mathematics, John Wiley & Sons Ltd., Chichester, 1997.

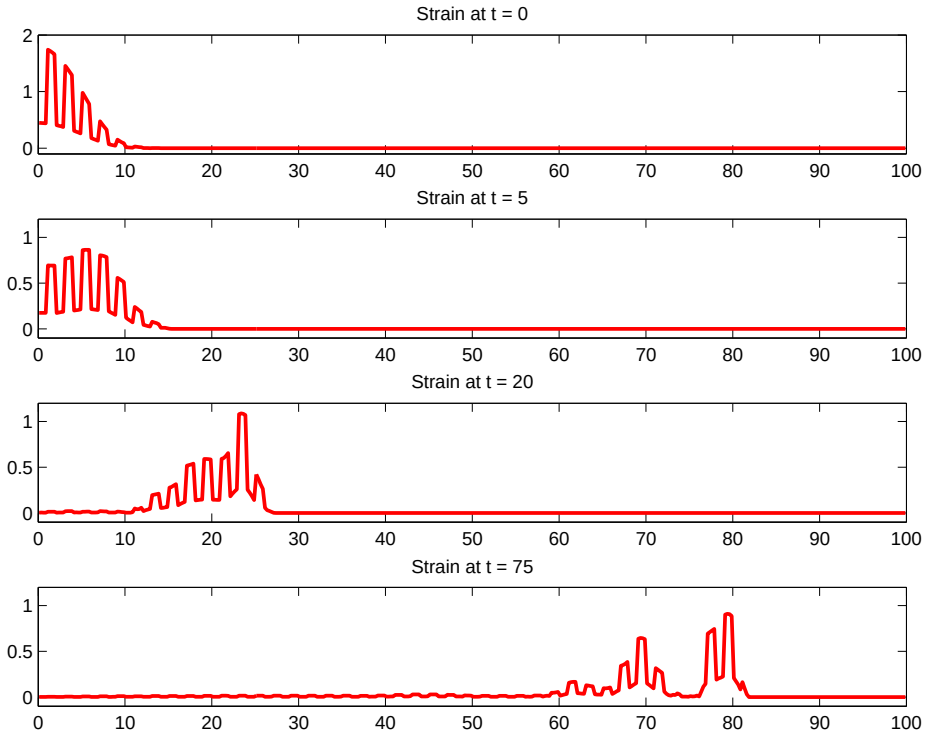

Figure 4.9: 2-D example. 1-D slices of strain at $y = 5$ at $t = 0, 5, 20, 75$ with $\Delta x = \Delta y = 0.25$.

[12] A. KURGANOV AND D. LEVY, *Central-upwind schemes for the Saint-Venant system*, M2AN Math. Model. Numer. Anal., 36 (2002), pp. 397–425.

[13] A. KURGANOV AND C.-T. LIN, *On the reduction of numerical dissipation in central-upwind schemes*, Commun. Comput. Phys., 2 (2007), pp. 141–163.

[14] A. KURGANOV, S. NOELLE, AND G. PETROVA, *Semi-discrete central-upwind scheme for hyperbolic conservation laws and Hamilton-Jacobi equations*, SIAM J. Sci. Comput., 23 (2001), pp. 707–740.

[15] A. KURGANOV AND G. PETROVA, *A second-order well-balanced positivity preserving central-upwind scheme for the Saint-Venant system*, Commun. Math. Sci., 5 (2007), pp. 133–160.

[16] A. KURGANOV AND G. PETROVA, *Central-upwind schemes for two-layer shallow equations*, SIAM J. Sci. Comput., 31 (2009), pp. 1742–1773.

[17] A. KURGANOV AND E. TADMOR, *New high resolution central schemes for nonlinear conservation laws and convection-diffusion equations*, J. Comput. Phys., 160 (2000), pp. 241–282.

[18] R.J. LEVEQUE, *Finite volume methods for hyperbolic problems*, Cambridge Texts in Applied Mathematics, Cambridge University Press, Cambridge, 2002.

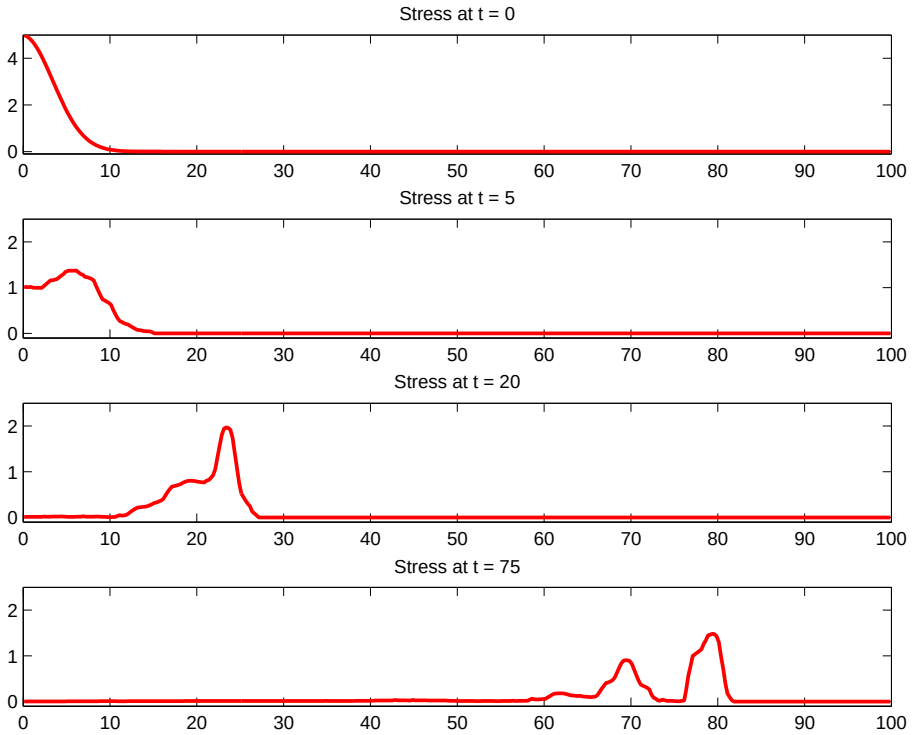

Figure 4.10: 2-D example. 1-D slices of stress at $y = 5$ at $t = 0, 5, 20, 75$ with $\Delta x = \Delta y = 0.25$.

[19] R. LEVEQUE, *Finite volume methods for non-linear elasticity in heterogeneous media*, Internat. J. Numer. Methods Fluids, 40 (2002), pp. 93–104.

[20] R. LEVEQUE AND T. FOGARTY, *High-resolution finite volume methods for acoustics in periodic or random media*, J. Acoust. Soc. Am., 106 (1999), pp. 17–28.

[21] R.J. LEVEQUE AND D.H. YONG, *Phase plane behavior of solitary waves in nonlinear layered media*, in Hyperbolic problems: theory, numerics, applications, Springer, Berlin, 2003, pp. 43–51.

[22] R.J. LEVEQUE AND D.H. YONG, *Solitary waves in layered nonlinear media*, SIAM J. Appl. Math., 63 (2003), pp. 1539–1560.

[23] D. LEVY, G. PUPPO, AND G. RUSSO, *Central WENO schemes for hyperbolic systems of conservation laws*, M2AN Math. Model. Numer. Anal., 33 (1999), pp. 547–571.

[24] K.-A. LIE AND S. NOELLE, *An improved quadrature rule for the flux-computation in staggered central difference schemes in multidimensions*, J. Sci. Comput., 63 (2003), pp. 1539–1560.

[25] K.-A. LIE AND S. NOELLE, *On the artificial compression method for second-order nonoscillatory central difference schemes for systems of conservation laws*, SIAM J. Sci. Comput., 24 (2003), pp. 1157–1174.

[26] X.-D. LIU AND E. TADMOR, *Third order nonoscillatory central scheme for hyperbolic conservation laws*, Numer. Math., 79 (1998), pp. 397–425.

[27] H. NESSYAHU AND E. TADMOR, *Nonoscillatory central differencing for hyperbolic conservation laws*, J. Comput. Phys., 87 (1990), pp. 408–463.

[28] L. PARESCHI, G. PUPPO, AND G. RUSSO, *Central Runge-Kutta schemes for conservation laws*, SIAM J. Sci. Comput., 26 (2005), pp. 979–999 (electronic).

[29] P.K. SWEBY, *High resolution schemes using flux limiters for hyperbolic conservation laws*, SIAM J. Numer. Anal., 21 (1984), pp. 995–1011.

[30] E.F. TORO, *Riemann solvers and numerical methods for fluid dynamics: A practical introduction*, Springer-Verlag, Berlin, Heidelberg, third ed., 2009.

[31] B. VAN LEER, *Towards the ultimate conservative difference scheme. V. A second-order sequel to Godunov's method*, J. Comput. Phys., 32 (1979), pp. 101–136.